Control of the flow around a finite square cylinder with a flexible plate attached at the free end

Hanfeng Wang(王汉封, wanghf@csu.edu.cn)[1, 2], Chongyu Zhao(赵崇宇, zhaochongyu@csu.edu.cn)[1],

Lingwei Zeng(曾令伟, lingwei.zeng@connect.polyu.hk)[1, 3*],

Md. Mahbub Alam(alam@hit.edu.cn)[4], Hui Tang(唐辉, h.tang@polyu.edu.hk)[3]

1 School of Civil Engineering, Central South University, Changsha, Hunan, China, 410075

2 National Engineering Laboratory for High-Speed Railway Construction, Changsha, Hunan, China, 410075

3 Research Center for Fluid-Structure Interactions, Department of Mechanical Engineering, The Hong Kong Polytechnic University, Kowloon, Hong Kong, China, 999077

4 Center for Turbulence Control, Harbin Institute of Technology (Shenzhen), Shenzhen, Guangdong, China, 518055

Abstract: A flexible plate vertically clamped at the free-end leading edge was used to modulate the aerodynamic forces on a wall-mounted finite square cylinder. The side width (d) of the cylinder was 40 mm and the aspect ratio (H/d) was 5. The flexible plate was made of low-density Polyethylene, with a width of d and thickness of 0.04 mm. The length of the flexible plate ranged from $d/8$ to d. All measurements were carried out in a low-speed wind tunnel with the free-stream velocity (U_∞) ranging from 4 to 20 m/s, corresponding to the Reynolds number ranging from 10960 to 54800. It was found that the flexible plate behaves distinctly depending on its length and has significant effects on the aerodynamic forces on the finite square cylinder. When U_∞ is smaller than the critical velocity U_{cr}, which is closely related to the length of the plate, the plate statically deforms, having a negligible influence on the aerodynamic forces on the cylinder. When U_∞ exceeds U_{cr}, the plate flaps periodically, resulting in a significant reduction in the aerodynamic forces. The maximum reduction in the mean drag, fluctuating drag and fluctuating lateral force reaches approximately 5%, 25% and 60%, respectively. The reduction in the aerodynamic forces is insensitive to both plate length and flapping frequency. Flow visualization and particle image velocimetry (PIV) results point out that the flapping plate induces large-scale vortices in the free-end shear flow, which suppress the formation of spanwise vortex shedding and make the upper part of the near wake symmetrical. The flapping configuration of the flexible plate and the corresponding pressure fluctuation on the

free end were also addressed.

Keywords: Finite square cylinder, Aerodynamic forces, Wake flow, Flow control, Flexible plate

Introduction

Flow around a wall-mounted finite square cylinder is characterized by the interaction between the spanwise shear flow, free-end downwash flow and possible upwash flow from the bottom wall, which makes the near wake highly three-dimensional and distinct from that of a 2D square cylinder (Bourgeois et al. 2011, 2012; McClean and Sumner, 2014; Wang and Zhou, 2009; Sohankar et al. 2018; Bai and Alam 2018; Rastan et al. 2021; Alam et al. 2020a; Abdelhamid et al. 2021). The free-end downwash flow and upwash flow are associated with the tip vortex and base vortex in the cylinder near wake, respectively (da Silva et al. 2020; Uffinger et al. 2013; Wang and Zhou, 2009). Wang and Zhou (2009) suggested that the free-end shear flow connects with the spanwise shear flow from both sides of the cylinder, forming an 'arch-type vortex structure' in the cylinder near wake. The tip vortex, spanwise vortex, and base vortex are all part of this arch-type vortex structure. The effects of aspect ratio H/d (where H and d are the cylinder height and width, respectively), Reynolds number Re, oncoming flow conditions, etc., on the flow around a finite square cylinder have been widely investigated (Kawamura et al. 2008; Sakamoto, 1985; Sakamoto and Arie, 1983; Wang et al. 2006; Zhao et al. 2021). Wang and Zhou (2009) found two most representative instantaneous configurations of this arch-type vortex structure: anti-symmetrical (Regime A) and symmetrical (Regime B) spanwise vortex shedding. A similar observation was also made by Bourgeois et al. (2011, 2012), Sattari et al. (2012) and Wang et al. (2017).

Besides the well-known periodic spanwise vortex shedding frequency, several investigations identified another low-frequency signature near the cylinder free end (Kindree et al. 2018; Peng et al. 2019). Sattari et al. (2012) suggested that this low-frequency behavior is associated with the shifting of spanwise vortex shedding between Regimes A and B, which may be modulated by the free-end shear flow. Kindree et al. (2018) found this low frequency is approximately 1/10 of the spanwise Karman vortex shedding. Moreover, the low-frequency pressure fluctuations on the two side faces of the cylinder are in-phase, while the high-frequency Karman vortex shedding is out of

phase. More recently, Peng et al. (2019) confirmed that this low-frequency behavior is connected to the up-down flapping of the free-end shear flow, which strongly correlates with the modes of spanwise vortex shedding. When the free-end shear flow flaps at its lower position, anti-symmetrical spanwise vortex shedding occurs. On the other hand, when it flaps at its upper position, symmetrical vortex shedding dominates, especially near the free end.

For the flow around a finite square cylinder, since the free-end shear flow connects the spanwise shear flow from both sides, it has significant effects on the entire near wake (Peng et al. 2019; Rastan et al. 2021). Park and Lee (2004) studied the effects of the free-end geometry on the near wake of a finite circular cylinder with $H/d = 6$. They found both beveled and radiused free end can suppress the separation bubble and reduce the width of the recirculation region in the near wake. For a wall-mounted short circular cylinder with $H/d = 1$, Rinoshika et al. (2017) connected its free end and rear part with an inclined hole, which allows the fluid to move from the near wake into the flow separation region above the free end. This additional connecting hole shrinks the separation region on the free end and also the recirculation bubble downstream the cylinder. For a finite square cylinder with $H/d = 5$, Wang et al. (2018) and Li et al. (2019) successfully utilized a steady slot suction at the free-end leading edge to suppress the fluctuating lateral force (46% achieved) and the vortex-induced vibration (VIV). More recently, Li et al. (2021) used a dual synthetic jet near the free-end leading edge to modulate the flow around a finite square cylinder with $H/d = 4$, and achieved more than 30% reduction in the fluctuating lateral force. These investigations confirmed that the proper local perturbation at the free end can yield remarkable modulation on the entire flow around a finite cylinder.

A vertically clamped flexible plate tends to flap periodically with large amplitude when the oncoming flow velocity U_∞ is larger than the critical velocity U_{cr}, which has significant potential applications in both flow control and energy harvesting systems (Fang et al. 2019; Brücker and Weidner, 2014; Chen et al. 2020; Doaré and Michelin, 2011; Lee et al. 2017; Orrego et al. 2017; Binyet et al. 2020). When $U_\infty < U_{cr}$, the flexible plate experiences a static reconfiguration, becoming more and more aligned to the freestream with increasing U_∞ and resulting in a significant drag reduction compared with a rigid plate with the same dimension (Alben et al. 2002; Gosselin et al. 2010; Leclercq et al. 2018). Once $U_\infty > U_{cr}$, the plate gets streaming and is prone to self-excited

oscillations, similar to what happens for a streamwise-aligned standard flag (Yu et al. 2019). The flapping plate results in large-scale vortices at its tip (Jin et al. 2018a, 2018b), which has been successfully applied in the enhancement in heat exchange in a channel flow (Chen et al. 2020; Joshi et al. 2015; Lee et al. 2017, 2018; Singh and Lakkaraju, 2019). Utilization of plate in flow control for bluff bodies dates to the study completed by Bearman (1965). The base pressure of a 2D bluff body with a blunt trailing edge can be reduced by approximately 60%, after the installation of a rigid splitter plate at its rear face. Anderson and Szewczyk (1997) found that the rigid splitter plate transmutes the classical Karman vortex into small-scale Bloor-Gerrard vortices by suppressing the transverse movement of spanwise shear layers. And then, a couple of studies were completed trying to improve aerodynamic performance of bluff bodies with a flexible plate attached at its leeward face (Niu and Hu, 2011; Wu et al. 2014a, 2014b; Sharma and Dutta, 2020). It is worth noting that flexible plate can also be used to suppress flow-induced vibration of bluff bodies (Liang et al. 2018). But all flow control strategies for 2D bluff bodies mentioned above are realized through modifications of spanwise vortices by introducing a splitter plate on the rear face. It is still unclear whether flexible plate is still applicable for modulating the flow around a 3D bluff body. So, it would be interesting to know how a vertically clamped flexible plate behaves in the free-end shear flow of a finite square cylinder, which can be considered as a typical representative of separated shear flows. Besides, it is worth investigating whether this flexible plate can efficiently modulate the flow around the cylinder.

This paper reports a systematic experimental investigation on the flow around and aerodynamic forces on a finite square cylinder with $H/d = 5$. A vertically clamped flexible plate is fixed at the free-end leading edge of the cylinder, with the plate length varying from $d/8$ to d. Instantaneous pressure distributions on the four side faces and free end are obtained to evaluate the effects of the flexible plate. Qualitative and quantitative flow visualizations are also conducted utilizing smoke wire and particle image velocimetry (PIV) to reveal the interaction mechanism between the flapping plate and near wake. Besides, a high-speed camera is also used to capture the flapping motion of the flexible plates in the free-end shear flow.

2 Experimental details

2.1 Experimental setup and oncoming flow conditions

All experiments were conducted in an open-circuit low-speed wind tunnel with a test section of 450 mm in width, 450 mm in height and 1200 mm in length. The freestream velocity can be adjusted continuously from 0 to 40 m/s, with the turbulence intensity lower than 0.5%. A finite square cylinder with H/d = 5, with its long axis normal to the incoming flow, was vertically mounted on a flat plate, as shown in figure 1. H and d were 200 mm and 40 mm, respectively. The flat plate was horizontally installed in the wind-tunnel test section, approximately 50 mm above the bottom wall. The leading edge of this plate was streamlined and polished to prevent flow separation. The blockage ratio caused by the tested cylinder was 4%, hence its effects would be neglected in the following discussions. The origin of the coordinate system was defined on the flat plate, as shown in figure 1(a). The x, y and z axis represented the streamwise, lateral and spanwise directions, respectively. In the experiment, U_∞ varied from 4 to 20 m/s, resulting in the Reynolds number, based on U_∞ and d, ranging from 8220 to 54800.

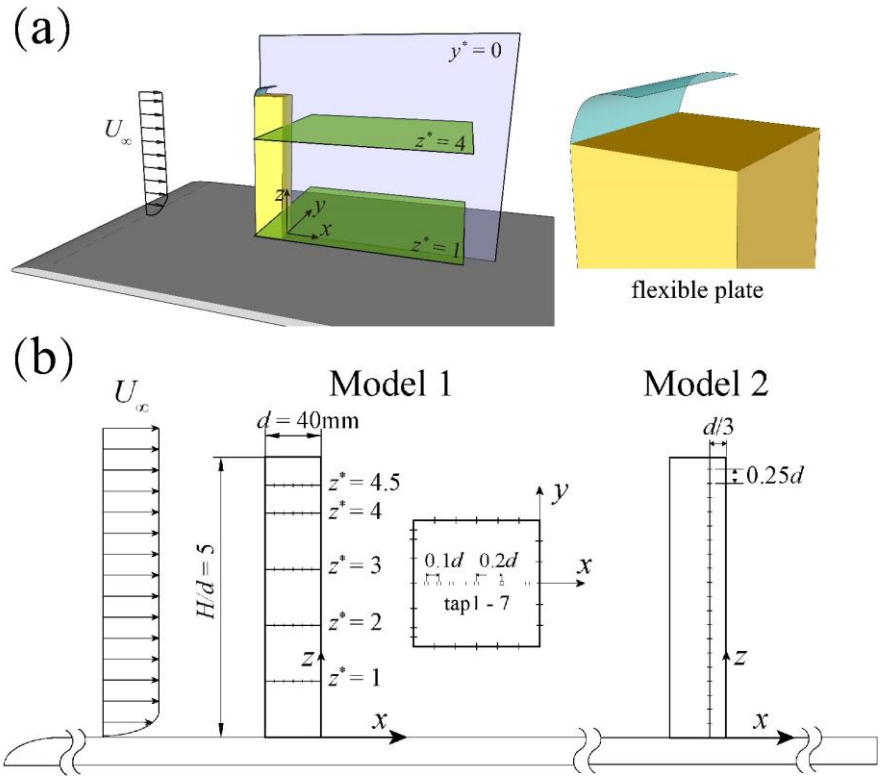

Figure 1 Experimental setup: (a) tested model and arrangement of PIV measurement planes; (b) distribution of pressure tabs.

The tested cylinder was placed 0.4 m downstream from the leading edge of the flat plate. The oncoming flow condition over the flat plate was documented using a Cobra probe (TFI, Series 100) at the position of the cylinder axis prior to its installation. The probe was moved along z direction using a traverse system with an accuracy of 0.01 mm. At each measurement point, the sampling duration of the probe was 20 s with a sampling frequency of 2 kHz. Figure 2 presents the time-averaged streamwise velocity $\overline{U^*}$ and streamwise turbulence intensity I_{uu} measured at U_∞ = 5, 10 and 15 m/s, respectively. Apparently, the distributions of both $\overline{U^*}$ and I_{uu} almost overlap at the three flow conditions, suggesting that the boundary layer over the flat plate was fully developed. The boundary layer thickness δ was 0.4 d. That is, the majority of the tested cylinder was in uniform flow with I_{uu} of approximately 0.4%, as shown in figure 2.

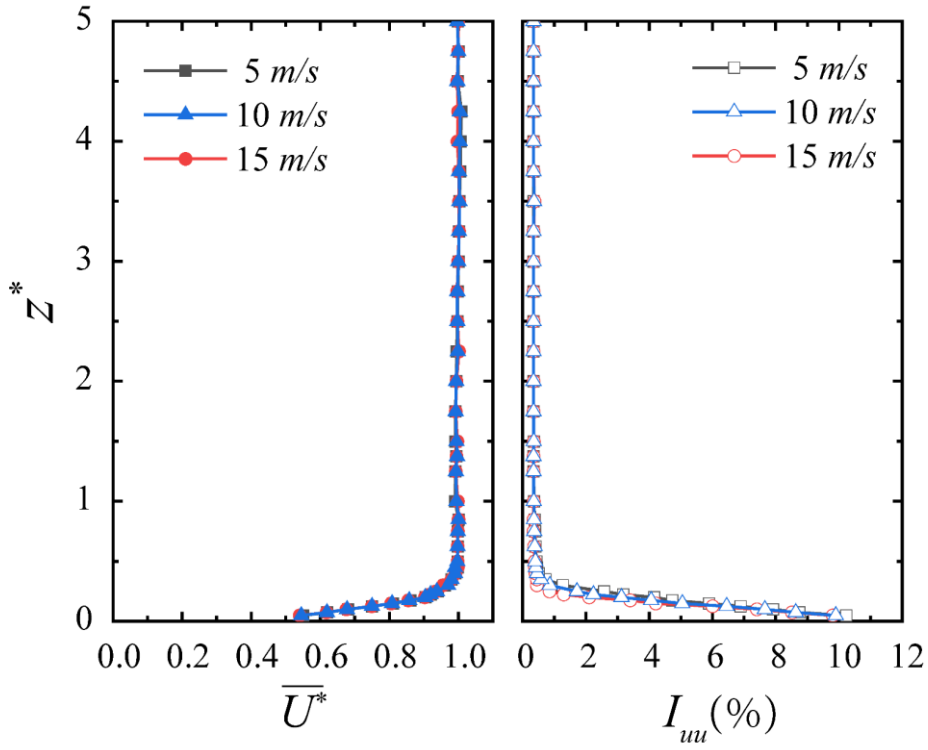

Figure 2 Oncoming flow conditions over the flat plate.

A flexible plate was vertically clamped at the leading edge of the free end of the cylinder, as shown in figure 1(a). This plate was made of low-density Polyethylene, with the density ρ_s of 0.91 g/cm^3 and flexural modulus E_s of 240 MPa. The thickness δ_s of the plate was 0.04 mm. The width of the plate was d, identical to that of the tested square cylinder. The dimensionless length l^* of the plate varied from 1/8 to 1 in the experiments, so that its influence on the aerodynamic forces of the

cylinder can be evaluated. The superscript '*' in the present paper indicates the normalization with U_∞ and/or d.

2.2 Measurement techniques

2.2.1 Aerodynamic forces

Two different models were used to measure the pressure distributions on the tested cylinder, as shown in figure 1(b), which were made of acrylonitrile butadiene styrene (ABS) using 3D printing. Model 1 was used to measure the circumferential pressure distribution at $z^* = 1$, 2, 3, 4 and 4.5. At each z^*, there were 22 pressure taps, with 7 on the front face and 5 on each of the side and leeward face, respectively, as shown in figure 1(b). Besides, there were another 7 taps arranged along the centerline of the free end, which were used to monitor the fluctuating pressure on the free end. For Model 2, two columns of pressure taps were arranged on the two side faces, at 2d/3 downstream from the vertical leading edge of the cylinder (figure 1b), where the pressure fluctuation is the strongest (Noda and Nakayama, 2003; Wang et al. 2017; Zhao et al. 2021). The pressure measured at these two columns of taps was used to determine the dominant frequency and phase relation of the spanwise vortex shedding. All pressure taps were connected to the pressure scanners (DTC Initium) using PVC tubes with an inner diameter of 0.8 mm and a length of 300 mm. The tap-tubing-scanner system had a frequency response of at least 100 Hz, which was higher enough than the dominant frequency of spanwise vortex shedding. The sampling frequency of the scanner was 333 Hz/channel, and the sampling duration for each test was 150 s.

The time-averaged pressure coefficient $\overline{C_p}$ and fluctuating pressure coefficient $C_p{}'$ were defined as follows:

$$\overline{C_p} = \frac{\overline{P} - P_\infty}{\frac{1}{2}\rho_f U_\infty^2}, \quad C_p^{'} = \frac{P^{'}}{\frac{1}{2}\rho_f U_\infty^2} \tag{1}$$

where $\bar{P}$ was the time-averaged pressure, $P^{'}$ was the root-mean-square value of the fluctuating pressure, P_∞ was the static pressure in the wind tunnel, obtained by a pitot tube connected with the pressure scanner, and ρ_f was the air density.

Coefficients of the overall aerodynamic forces were defined as follows:

$$\overline{C_d} = \frac{\overline{F_d}}{\frac{1}{2}\rho_f U_\infty^2 A},\quad C_d^{'} = \frac{F_d^{'}}{\frac{1}{2}\rho_f U_\infty^2 A},\quad C_l^{'} = \frac{F_l^{'}}{\frac{1}{2}\rho_f U_\infty^2 A} \tag{2}$$

where $\overline{F_d}$, $F_d^{'}$ and $F_l^{'}$ were the time-averaged drag, root-mean-square values of the fluctuating drag and fluctuating lateral force, respectively. $A=Hd$, is the streamwise projection area of the finite cylinder. The overall aerodynamic forces were estimated from the circumferential pressure measured at $z^* = 1$, 2, 3, 4 and 4.5, identical to those in Peng et al. (2019) and Zhao et al. (2021).

2.2.2 Near-wake flow field

The near wake of the cylinder was visualized both qualitatively and quantitatively using smoke wire and 2D particle image velocimetry (PIV), respectively. As shown in figure 1(a), the PIV measurement was conducted in the spanwise planes at $z^* = 1$ and 4, and the lateral plane at $y^* = 0$. For each measurement plane, a total of 2000 image pairs were captured at a rate of 5 Hz. The resolution of the CCD camera of the PIV was 2560 × 2160 pixel^2 while the spatial resolution of the present PIV measurement was 112 μm/pixel. 32 × 32 pixel^2 interrogation windows with a 50% overlap in both directions were utilized in the subsequent cross-correlation analysis. That is, the actual size of the interrogation window was about 3.58 mm × 3.58 mm (approximately 0.09d × 0.09d). Tracing particles used for the PIV measurement were atomized paraffin using a pressure nozzle. The diameter of the tracing particles was about 1-5 μm. Flow visualization was also conducted in the planes identical to the PIV measurement using smoke wire technique.

2.2.3 Behavior of the flexible plate

The behavior of the flexible plate was recorded by a high-speed camera (Photron FASTCAM Mini UX50) at a shooting frequency of 2000 frames per second. A flicker-free LED spotlight was used to provide sufficient illumination. Based on the video recording, it was easy to determine the flapping frequency and configuration of the plate.

To associate the plate flapping with the pressure fluctuation on the cylinder free end, the field of view was also illuminated using the pulsing laser sheet identical to that used in the PIV measurement. The instantaneous pressure fluctuation was monitored by a pressure transducer at the center of the free end. The triggering signal of the laser and the instantaneous pressure signal were sampled simultaneously, as shown in figure 3(a). The high-speed camera captured the image only

when the pulsing laser sheet illuminated the field of view, as shown in figure 3(b). Thus, the pressure fluctuation on the cylinder free end could be associated with the flapping behavior of the plate, which will be discussed in detail in the following sections.

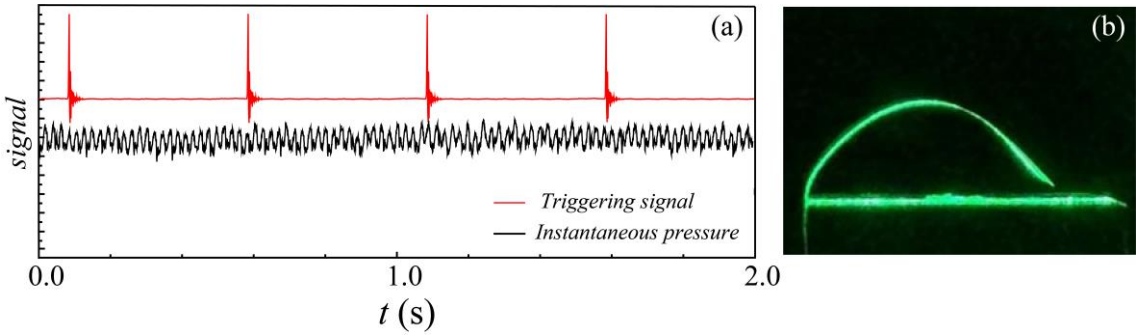

Figure 3 Instantaneous signals of the pressure transducer and laser triggering signal and typical image of the flexible film: (a) instantaneous signals; (b) image of the flapping film.

3 Results and discussion

3.1 Aerodynamic characteristics of the cylinder

The drag of the finite cylinder was obtained by integrating the pressure, as introduced in section 2.2.1, which does not include the drag acting on the flexible plate. It is necessary to evaluate this additional drag induced by the plate. For a cantilevered flexible plate in cross flow, as shown in figure 1(a), two typical states will occur with increasing U_∞ (Gosselin et al. 2010), i.e., steady deformation and flapping. The drag experienced by a flexible plate is much lower than if it is rigid, because of the reconfiguration which makes it more streamlined and the reduction of its projected area on cross flow plane (Leclercq et al. 2018). Two parameters were proposed to describe the dependence of the drag experienced by a flexible plate under steady deflection on U_∞, i.e., the reconfiguration number R and the scaled Cauchy number $\widetilde{C_Y}$,

$$R = \frac{F_D}{\frac{1}{2}\rho_f LW\overline{C_{dp}}U_\infty^2} \tag{3}$$

$$C_Y = C_D\frac{\rho_f L^3 U_\infty^2}{2B} \tag{4}$$

where F_D is the mean drag force on the flexible plate, $\overline{C_{dp}}$ is the mean drag coefficient of a rigid plate with the same dimensions, and B is the flexural rigidity of the plate. R indicates the effect of plate deformation on its mean drag when compared to a case of a rigid plate with the same

dimensions. $\widetilde{C_Y}$ reflects the competition between the forces induced by the oncoming flow and the resistance of the plate. Gosselin et al. (2010) found that the dependence of R on $\widetilde{C_Y}$ for different flexible plates and fibers followed a unified trend (see figure 5 of Gosselin et al. 2010). Following this idea, it is easy to estimate the mean drag of the steady deformed plate in the present experiment. Taking the case with $l^* = 1/2$ for instance, the critical U_∞ at which the flexible plate starts flapping is approximately 7.3 m/s (which will be discussed in detail later), and the $\overline{C_{d\mathrm{p}}}$ of a rigid plate with the same dimensions is 1.19 (Gosselin et al. 2010). That is, $\widetilde{C_Y}$ is 44129 and the corresponding R is 0.045, which means the mean drag coefficient of the flexible plate can be estimated as $\overline{C_{d\mathrm{p}}} \cdot R$, i.e., 0.054, which is negligibly small relative to the $\overline{C_d}$ of the tested finite square cylinder (Leclercq et al. 2018). Similarly, for $l^* = 1$, its mean drag coefficient is approximately 0.085, also far smaller than $\overline{C_d}$. Although the mean drag coefficient of a flexible plate increases slightly when it starts flapping, it is never large enough to offset the significant drag reduction due to its reconfiguration (Leclercq et al. 2018).

As for the additional fluctuating drag induced by the flapping plate, it can also be estimated similarly. The reconfiguration number R depends on the flapping modes of the flexible plate (Leclercq et al. 2018). In the present research, the flexible plate is always in the periodic flapping mode because of the strong periodicity of pressure on the cylinder free end. So, it can be confirmed that the reconfiguration number R increases very slightly after flapping. Take the case with $l^* = 1/2$ for instance, the $\widetilde{C_Y}$ is 44129 and the corresponding maximum value of R may be 0.06 after flapping. Based on Leclercq et al. (2018)'s theoretical analysis, the maximum instantaneous drag coefficient experienced by the flapping plate is about 0.072. Thus, the maximum fluctuating drag is 0.018, after the subtraction of the corresponding mean value of 0.054. Consequently, we may estimate the rms value of the fluctuating drag based on the corresponding mean and maximum, if we assume the instantaneous drag approximates Gauss distribution. The estimated rms value of the fluctuating drag is approximately one third of this maximum, i.e., about 0.006, which is one order smaller than that of the fluctuating drag of the bare cylinder, 0.06. As for the case with $l^* = 1$, the rms value of fluctuating drag is only about 0.004, also far smaller than the corresponding value of the cylinder. Thus, the present paper focuses only on the influences of the flapping plate on the cylinder, including flow structure and aerodynamics forces, especially the fluctuating lateral force.

Figure 4 presents the overall aerodynamic force coefficients of the finite square cylinder with a flexible plate at its free end with l^* ranging from 0 to l. The $l^* = 0$ is the uncontrolled case, serving as a benchmark for comparison. For the uncontrolled case, $\overline{C_d}$, C_d' and C_l' are 1.65, 0.06 and 0.12, respectively, and remain almost unchanged with increasing U_∞ from 4 to 20 m/s. For a wall-mounted finite cylinder, its aerodynamic forces are sensitive to the oncoming flow conditions, e.g., boundary layer thickness on the bottom wall and free-stream turbulence intensity (Wang et al. 2017; Zhao et al. 2021). The presently measured $\overline{C_d}$, C_d' and C_l' are very close to those reported by Wang et al. (2018) with similar flow conditions, confirming the validation of the present measurement results.

For the case with $l^* = 1/8$, $\overline{C_d}$, C_d' and C_l' also remain almost unchanged with increasing U_∞. However, both $\overline{C_d}$ and C_l' are slightly larger than their corresponding values in the uncontrolled case, which may be ascribed to the fact that within the present U_∞ range, the flexible plate with $l^* = 1/8$ is always statically deformed, bending along the free-end shear flow. This statically deformed plate acts to upraise the free-end shear flow, which is equivalent to a slightly increased aspect ratio of the finite cylinder.

For the cases with $l^* \geq 1/4$, the aerodynamic forces, especially C_d' and C_l', reduce significantly with increasing U_∞. Generally, at a relatively smaller U_∞, C_d' and C_l' are slightly larger than their corresponding values in the uncontrolled case, the mechanism of this observation is similar with that for the case with $l^* = 1/8$. Once U_∞ reaches the critical velocity U_{cr}, C_l' reduces sharply and reaches another stable value with increasing U_∞, as shown in figure 4(c). U_{cr} is the critical velocity at which the flexible plate starts flapping, which reduces with increasing l^*. It is worth mentioning that, for the case with $l^* = 1$, there is no obvious reduction in C_l' within the present U_∞ range, since the plate has already started flapping at $U_\infty < 4$ m/s. Consequently, the C_l' for the case with $l^* = 1$ is always far smaller than that for the uncontrolled case.

For all the cases with $l^* \geq 1/4$, the maximum reduction in C_l' at $U_\infty > U_{cr}$ is approximately 60% (figure 4c), suggesting that the flapping plate may substantially suppress the alternate vortex shedding. Similarly, C_d' also reduces considerably once $U_\infty > U_{cr}$, as shown in figure 4(b). The maximum reduction in C_d' ranges approximately from 17% to 38% for different l^*, relatively smaller than the reduction in C_l'. A close look at figure 4(a) can reveal that, accompanied by the reduction in C_d' and C_l', $\overline{C_d}$ also reduces slightly once the flexible plate flaps, though its maximum reduction

is approximately 5% relative to the uncontrolled case.

As shown in figure 4, $\overline{C_d}$, C_d' and C_l' of the finite square cylinder strongly depend on the status of the flexible plate. The behaviors of the flexible plate with $l^* = 1/4$ and 1 at several typical U_∞, captured by the high-speed camera, are supplemented in figure 4(c). The corresponding symbols of C_l' is filled and enlarged for easy recognizing. When $U_\infty < U_{cr}$, the plate is statically deformed along the wind, acting to uplift the free-end shear flow and thus slightly enhancing the aerodynamic forces. Once $U_\infty > U_{cr}$, the plate starts flapping, and $\overline{C_d}$, C_d' and C_l' reduce significantly and reach a smaller stable value with increasing U_∞, regardless of l^*. Generally, the flexible plate flaps with a more complex mode with increasing U_∞, as shown in figure 4(c). Obviously, the maximum reductions in $\overline{C_d}$, C_d' and C_l' are not sensitive to the flapping mode of the plate. Leclercq et al. (2018) suggested that the switch of the flapping mode continues with increasing U_∞, which is accompanied by the loss of periodicity, i.e., from highly periodic to quasiperiodic. Considering these remarkable effects of the flexible plate on the overall forces of the finite cylinder, it is of interest to examine the sectional forces at different heights and the pressure distribution on the cylinder surfaces, which may highlight the mechanism of the reduction in aerodynamic forces.

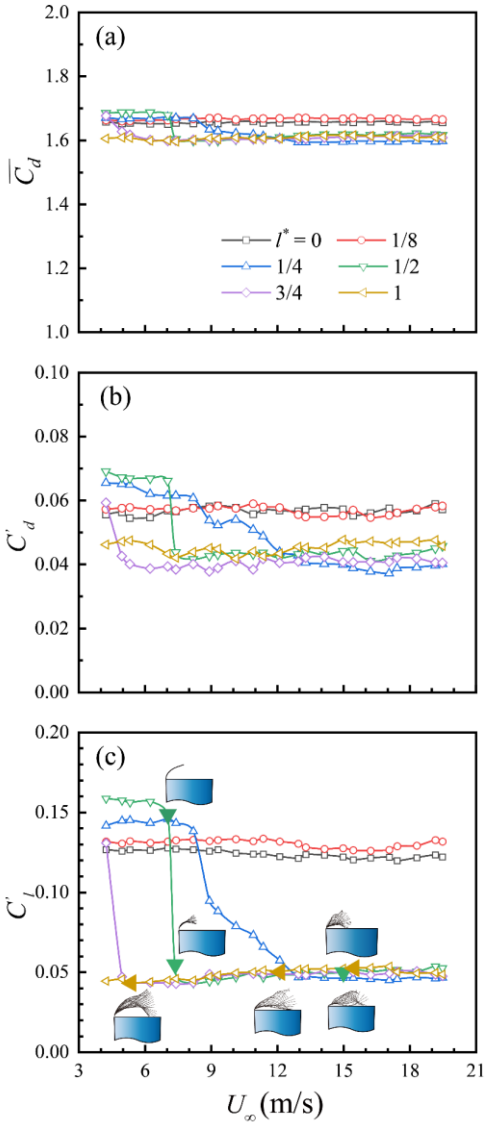

Figure 4 Overall aerodynamic forces of the finite cylinder with a flexible film at its free end: (a) $\overline{C_d}$, (b) C_d' and (c) C_l'.

Figure 5 presents the sectional aerodynamic forces along the cylinder height at U_∞ = 15 m/s. The plate with all l^* values, except the one with l^* = 1/8, flaps at this U_∞, which can be read from figure 4. For l^* = 0, $\overline{C_d}$, C_d' and C_l' are obviously not uniform along the span, although the majority part of the cylinder is in the uniform oncoming flow (see figure 2). The $\overline{C_d}$ is the largest near the free end and reduces gradually toward the bottom wall. This observation is similar to that reported by Okamoto and Yagita (1973) and Wang et al. (2018) for both finite circular and square cylinders. Farivar (1981) ascribed this to the free-end downwash flow, which results in lower backpressure near the cylinder tip. The maximum C_d' also presents at z^* = 4.5, very close to the free end. Wang

et al. (2018) suggested the larger C_d' near the free end is caused by the flapping of the free-end shear flow. Contrary to C_d', C_l' is the smallest near the free end and increases monotonically with reducing z^*. This is ascribed to the fact that C_l' is dominated by the alternating spanwise vortex shedding, which is substantially weakened near the free end because of the free-end downwash flow.

For the case with $l^* = 1/8$, $\overline{C_d}$, C_d' and C_l' at all spanwise locations are slightly larger than their corresponding values for the uncontrolled case, because the steady deformed plate at the free end acts to uprise the free-end shear flow, which is equivalent to increase the cylinder aspect ratio to some extent. Contrarily, for the cases with $l^* > 1/4$, the plate flaps at $U_\infty = 15$ m/s and modulates the aerodynamic forces remarkably at all spanwise locations. Generally, the reduction in $\overline{C_d}$ is smaller than that in C_d' and C_l', although it is relatively larger near the free end and cylinder base. For the case with $l^* = 1/4$, C_d' reduces by 30% ~ 40% along the entire height, as shown in figure 5(b). Interestingly, C_d' at the upper half of the cylinder, especially near the free end, enlarges with increasing l^*. At $z^* = 4.5$, C_d' for the case with $l^* = 1$ eventually exceeds that for the uncontrolled case. This is ascribed to the higher fluctuating pressure on the leeward surface of the cylinder because of the flapping of the relatively long flexible plate, which will be discussed in detail later. Contrary to the behavior of $\overline{C_d}$ and C_d', C_l' presents a more remarkable reduction for the cases with $l^* > 1/4$, especially at the lower half of the cylinder, which exceeds 60% at $z^* = 1$.

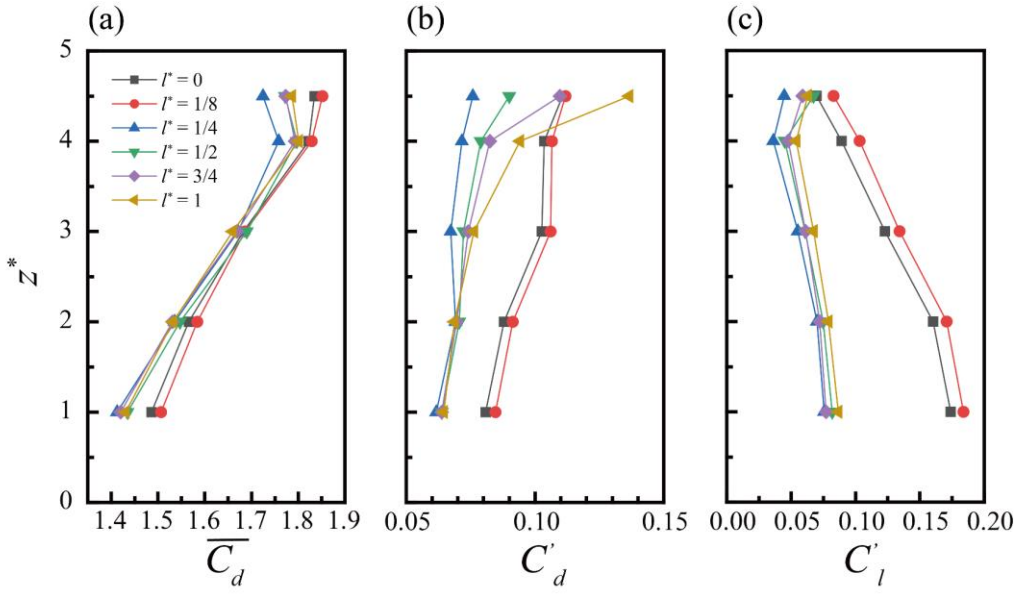

Figure 5 Sectional aerodynamic forces of the finite cylinder at $U_\infty = 15$m/s:

(a) $\overline{C_d}$, (b) C_d' and (c) C_l'.

The sectional aerodynamic forces shown in figure 5 suggest that a flexible plate at the cylinder free end not only changes the forces near the free end, but also modulates those along the entire height. Consequently, it is interesting to look at the distribution of $\overline{C_p}$ and C_p' on the cylinder surfaces at U_∞ = 15 m/s, as shown in figure 6.

For the uncontrolled case, since the majority of the cylinder is immersed in the uniform oncoming flow, the $\overline{C_p}$ distribution on the windward surface is uniform along the spanwise direction. On the contrary, $\overline{C_p}$ on the leeward face reduces (more negative) gradually with increasing z^*, suggesting that the non-uniform $\overline{C_d}$ along z direction (figure 5a) is largely associated with the non-uniform $\overline{C_p}$ on the leeward face, similar to that found by Rastan and Alam (2021) using large eddy simulation (LES). If the finite square cylinder is fully immersed in a turbulent boundary layer, $\overline{C_p}$ on the windward surface increases toward the free end, since U_∞ enlarges with increasing z^* within the turbulent boundary layer (Kikuchi et al. 1997; Wang et al. 2017; Zheng and Zhang, 2012). That is, the non-uniform $\overline{C_p}$ on both windward and leeward surfaces contributes to the variation of $\overline{C_d}$ along the z direction.

For the uncontrolled case, C_p' on the windward face is very small compared with that on the side and leeward faces involving flow separation and vortex shedding, respectively. The maximum C_p' appears near the vertical trailing edges of the cylinder, which is postponed relative to the case of a two-dimensional (2D) square cylinder. For the latter, Noda and Nakayama (2003) found that the maximum C_p' appears at approximately d/3 upstream from the vertical trailing edge, where the spanwise vortex develops completely and flaps on the side faces. Besides, the maximum C_p' of the finite cylinder is approximately 0.12, as shown in figure 6, which is approximately 1/5 of that of a 2D square cylinder (Noda and Nakayama, 2003; Wang et al. 2017). This suggests that the spanwise vortex shedding of a finite square cylinder is substantially suppressed compared with that of a 2D one. Besides, the downwash flow and upwash flow in the highly three-dimensional wake of the finite square cylinder weakens the C_p' near the free end and cylinder base, resulting in an H-shape distribution of C_p' on the leeward face (Kikuchi et al. 1997).

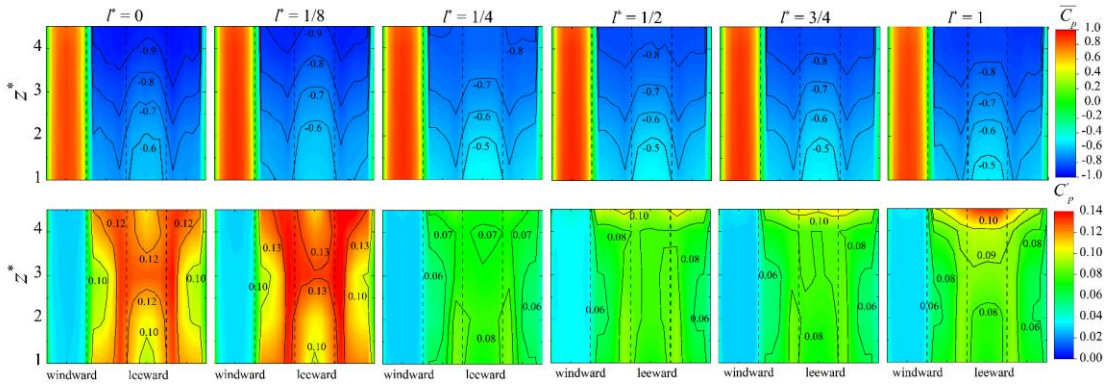

Figure 6 Contours of $\overline{C_p}$ and C_p' on the finite cylinder at U_∞ = 15 m/s.

For the case with l^* = 1/8, the distributions of $\overline{C_p}$ and C_p' are very similar to those of the uncontrolled case, except for the slightly enhanced C_p', as shown in figure 6. This observation is consistent with that on figures 4 and 5. That is, the steady deformed plate at the free end acts to uplift the free-end shear flow, increasing the effecting aspect ratio of the cylinder, and thus enhancing the spanwise vortex shedding.

The distributions of $\overline{C_p}$ and C_p' for the cases with l^* = 1/4, 1/2, 3/4 and 1 are completely different from those for the uncontrolled case, as shown in figure 6. Several observations can be made: First, although $\overline{C_p}$ on the windward face is almost unchanged, a flapping plate at the free end slightly raises the backpressure, regardless of l^*, which results in the reduction in $\overline{C_d}$, as shown in figures 4 and 5. Second, C_p' on the side and leeward faces reduces obviously compared with the uncontrolled case, suggesting that the flapping plate suppresses the spanwise vortex shedding significantly. Third, C_p' near the cylinder free end, especially on the leeward face, increases gradually with increasing l^*, which is associated with the enhanced sectional C_d' near the free end (figure 5b). For the case with l^* = 1, the maximum C_p' reaches 0.12, exceeding that near the vertical trailing edges dominated by the spanwise vortex shedding.

Both Kindree et al. (2018) and Peng et al. (2019) found that the spanwise shear flow and associated fluctuating lift of a finite square cylinder have a remarkable low-frequency instability with a frequency of about 1/10 of the well-known spanwise Karman vortex shedding, which results from the flapping of the free-end shear flow (Peng et al. 2019). Figure 7 presents the time histories of lift coefficient C_l, pressure coefficient C_{p4d} at z^* = 4 (2d/3 downstream from the leading edge) and pressure coefficient $C_{p\mathrm{T}}$ at the center of the free end and their corresponding spectra at U_∞ = 15

m/s. For the uncontrolled case, the two typical vortex shedding modes (Kindree et al. 2018; Peng et al. 2019), i.e., alternate spanwise vortex shedding with high-amplitude fluctuating C_l and co-shedding spanwise vortex with low-amplitude fluctuating C_l, are clearly observed, as shown in figure 7(a). The switch between these two typical modes correlates with the low-frequency fluctuation of both C_{p4d} and $C_{p\mathrm{T}}$, which corresponds well with that reported by Peng et al. (2019). The spectrum of C_l presents its dominant peak at $f_s^* = 0.11$ that corresponds to the spanwise Karman vortex shedding. This f_s^* is slightly smaller than its counterpart for a 2D square cylinder, because the free-end downwash flow tends to keep the spanwise shear flow separated and postpones the Karman vortex shedding (Wang & Zhou, 2009). The spectrum of C_{p4d} presents two peaks, as shown in figure 7(c). The peak at $f_s^* = 0.11$, resulted from the spanwise Karman vortex shedding, is very weak because the flow around the cylinder free end is highly three-dimensional and tends to attenuate the spanwise Karman vortex shedding (Wang et al. 2017). Besides, there is a broad-band low-frequency peak at $f^* \approx 0.01$ (as highlighted in figure 7c), approximately 1/10 of the spanwise Karman vortex shedding, which is identical to those reported by Kindree et al. (2018) and Peng et al. (2019). This observation suggests, besides the Karman vortex shedding, spanwise shear flow near the free end is also dominated by the low-frequency flapping of the free-end shear flow. As expected, the spectrum of $C_{p\mathrm{T}}$ has only the low-frequency peak associated with the flapping of free-end shear flow (figure 7c), without any trace of the influence of Karman vortex shedding.

For the case with $l^* = 1$ at $U_\infty = 15$ m/s, the periodic fluctuation of C_l is substantially suppressed relative to the uncontrolled case (figure 7b), resulting in the weakened peak in its power spectrum (figure 7d). This is consistent with figures 4 and 5, suggesting that the flapping plate at the free end attenuates the Karman vortex shedding. Since the plate flaps at $U_\infty = 15$ m/s, see the sketch in figure 4(c) for reference, $C_{p\mathrm{T}}$ presents violent fluctuation, as shown in figure 7(b). Its spectrum presents a pronounced peak at $f_p^* = 0.22$. It is worth mentioning that $f_p^* = 0.22$ is the flapping frequency of the plate, not the harmonic of the spanwise Karman vortex shedding, although it is coincidentally twice of the latter. The flapping frequency of the flexible plate associates with l^* and U_∞, which will be addressed later in section 3.2. The spectrum of C_{p4d} also presents a remarkable peak at $f_p^* = 0.22$. Besides, the low-frequency peak in the spectra of C_{p4d} and $C_{p\mathrm{T}}$, caused by the natural flapping of free-end shear flow (figure 7c), disappears in figure 7(d). This observation indicates that, instead of

the natural low-frequency flapping of the free-end shear flow, the flapping plate at the cylinder free end can modulate this free-end shear flow completely, and thus has a significant influence on the aerodynamic forces of the finite cylinder.

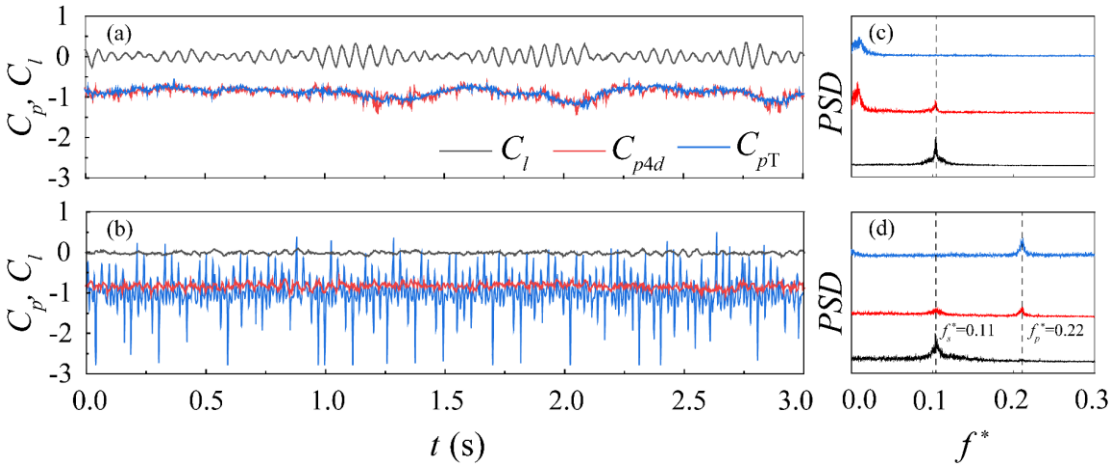

Figure 7 Time history of C_l, C_{p4d} and C_{pT} and their corresponding spectra at U_∞ = 15 m/s: (a, c) uncontrolled case, (b, d) l^* = 1.

3.2 Flapping behavior of the flexible plate

Since the flapping flexible plate at the free end modulates the aerodynamic forces on the finite cylinder considerably, as discussed in section 3.1, it is of interest to look at its flapping behavior and the associated pressure fluctuation on the cylinder free end.

Taking advantage of the technique described in section 2.2.3, the flapping position of the plate can be synchronized with the pressure fluctuation. Figure 8 presents the typical flapping motion of the plate with l^* = 1 at U_∞ = 8 m/s. The corresponding fluctuating pressure c_{pT} at the center of the free end is indicated by the colored dot at the tip of each solid line. The c_{pT} is defined as $c_{pT} = C_{pT} - \overline{C_{pT}}$, where C_{pT} and $\overline{C_{pT}}$ are the instantaneous and time-averaged pressure at the free-end center, respectively. Note that, only the selected typical flapping configurations of the plate are shown in figure 8 for easy data interpretation. The trajectory of the plate tip looks like a teardrop. The plate is more curved during flapping upwards than flapping downwards, as shown in figure 8. The flapping motion of the plate dominates the variation of c_{pT}. Particularly, the minimal and maximal c_{pT} appear at the initial stages of the upward and downward flapping motion, respectively. This observation suggests that c_{pT} tends to be negative when the plate flaps upwards and vice versa. Apparently, the flapping frequency of the plate can be determined by the fluctuation of c_{pT}, which

will be discussed later.

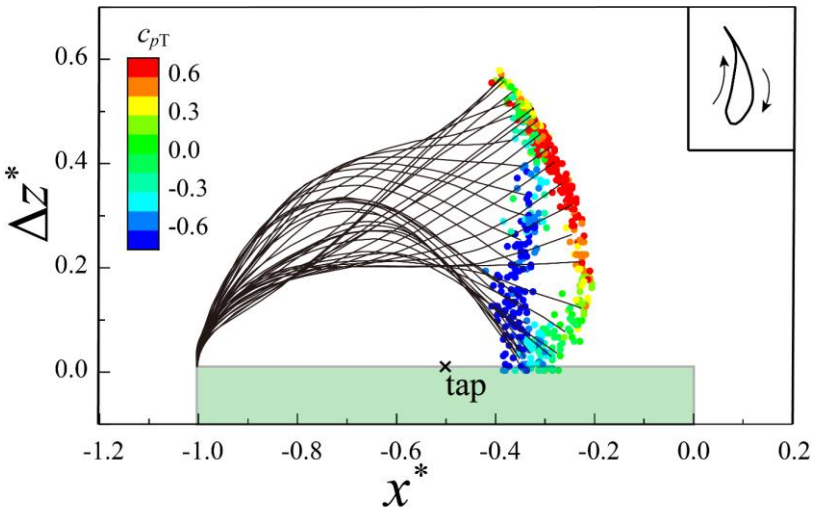

Figure 8 Typical flapping configurations of the flexible film with $l^* = 1$ at $U_\infty = 8$ m/s. The endpoint of the film is colored by the corresponding c_{pT}.

Figure 9 presents the $C_p^{'}$ at the seven pressure taps on the free end (as shown in figure 1b) at typical U_∞. For the uncontrolled case at $U_\infty = 5$ and 8 m/s, $C_p^{'} \approx 0.13$-0.14, and is approximately uniform along the streamwise direction (figure 9a), which can be ascribed to the fact that the free end is completely immersed in the relatively stable recirculation bubble formed by the free-end shear flow (Rastan et al. 2017; Sumner et al. 2017; Wang et al. 2020). Note that, $C_p^{'}$ is almost independent of U_∞ for the uncontrolled cases, suggesting that the free-end shear flow is insensitive to U_∞ for the uncontrolled case.

For the case with $l^* = 1/2$, $C_p^{'}$ differs between $U_\infty = 5$ and 8 m/s, as shown in figure 9(b). At $U_\infty = 5$ m/s, the flexible plate is steady bended along the streamwise direction, as indicated by the solid blue line, which apparently does not have any noticeable effects on $C_p^{'}$, compared with that for the uncontrolled case. It suggests that a steady deformed flexible plate at the free end does not have any obvious effects on the free-end shear flow, which is consistent with the results shown in figure 4. When $U_\infty = 8$ m/s, the flexible plate flaps periodically. The red area indicates the flapping boundary of the plate, as shown in figure 9(b). Apparently, once the plate flaps, $C_p^{'}$ on the free end becomes far larger than that of the uncontrolled case and the case with the flexible plate steady deformed. The $C_p^{'}$ increases gradually along the streamwise direction with its maximum appearing at the position slightly downstream where the tip of the flapping plate reaches, as shown in figure

9(b). With moving further downstream, $C_p^{'}$ reduces quickly to approximately 0.3, twice of the uncontrolled cases, near the trailing edge of the free end. The distribution of $C_p^{'}$ suggests that the flapping plate may generate detached vortices at its tip, which impinge on the cylinder free end and result in the higher $C_p^{'}$.

For $l^* = 1$, the flexible plate flaps at $U_\infty = 5$ and 8 m/s with the corresponding flapping boundary indicated by the blue and red area, respectively, as shown in figure 9(c). It is not unexpected, the flapping plate becomes more streamwise deformed with increasing U_∞, with a larger tip area touching the cylinder free end. However, the distributions of $C_p^{'}$ are still qualitatively similar for these two typical U_∞ values. Particularly, as shown in figure 9(c), $C_p^{'}$ increases along the streamwise direction with its maximum near the free-end trailing edge. Comparing with $C_p^{'}$ of $l^* = 1/2$ at $U_\infty = 8$ m/s (figure 9b), it may be concluded that the detached vortices from the flapping plate with $l^* = 1$ may form slightly downstream the trailing edge of the cylinder free end.

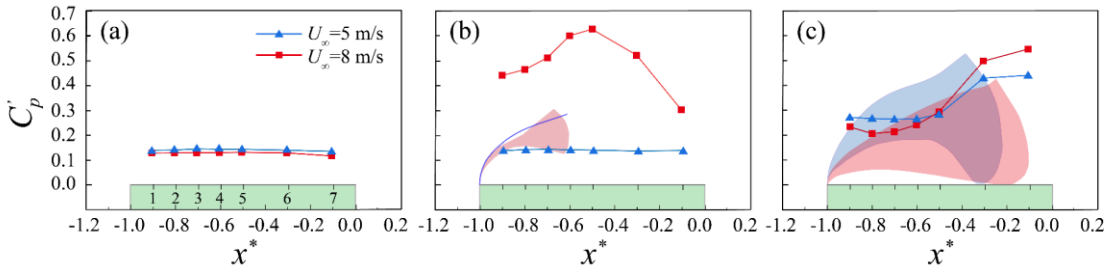

Figure 9 $C_p^{'}$ on the cylinder free end at $U_\infty = 5$ and 8 m/s, (a) uncontrolled case, (b) $l^* = 1/2$ and (c) $l^* = 1$.

Figure 10 gives the filtered instantaneous pressure c_p at the seven taps on the free end (see figure 1b). Since c_p is dominated by the flapping of the plate, it exhibits strong periodicity as shown in figure 7 (b & d). In order to highlight these periodic features, c_p in figure 10 is filtered with a 3 Hz frequency band centered at the dominating flapping frequency of the plate. As expected, c_p at all taps present significant periodicity associated with the flapping frequency. However, they are not in-phase, especially for the c_p near the trailing edge of the free end. Taking c_p at tap 1 (near the leading edge of the free end, see figure 1b) as a reference, the phase difference $\Delta\varphi$ between taps 2-7 and tap 1 can be quantified, as shown in figure 10 (c & d). For the case with $l^* = 1/2$ (figure 10c), $\Delta\varphi$ is approximately zero at taps 2 – 5, suggesting c_p at these taps are all synchronized with the flapping plate. The $\Delta\varphi$ enlarges (in magnitude) rapidly with increasing x^*, exceeding $-\pi/4$ and $-3\pi/4$

at taps 6 and 7, respectively. This observation suggests that the flapping plate dominates and synchronizes the pressure at taps 1-5, while the detached vortex from the tip of the plate is formed on the downstream part of the free end and moves along x direction, resulting in the phase lag at taps 6 and 7. Qualitatively similar observation can also be found for the case with $l^* = 1$ (figure 10d), except that the obvious phase lag presents only at tap 7. This is expected since the detached vortex is formed further downstream for $l^* = 1$ compared with that for $l^* = 1/2$, more pressure taps are dominated and synchronized by the flapping plate for $l^* = 1$.

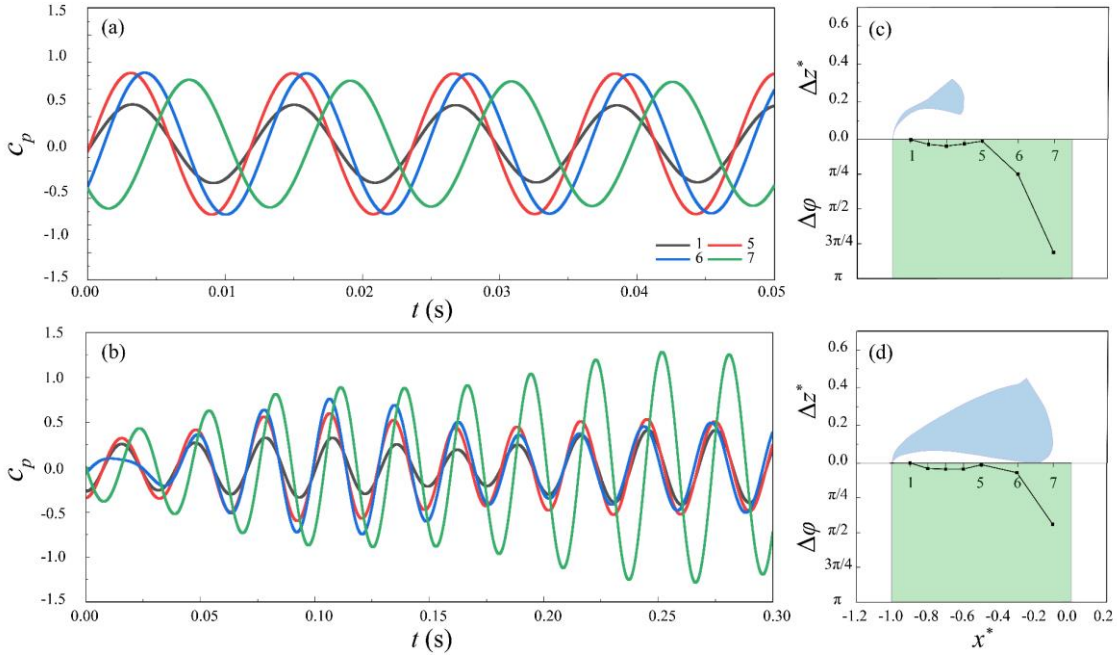

Figure 10 Fluctuating pressure c_p on the cylinder free end and their phase relation at U_∞ = 8 m/s: (a, c) $l^* = 1/2$, (b, d) $l^* = 1$.

Two approaches are applied to obtain the onset velocity U_{cr} and the frequency f_p of the flapping plate. Because of the direct connection between the flapping motion of the plate and the c_p on the free end (figure 8), both U_{cr} and f_p of the plate can be determined by analyzing c_p via Fast Fourier Transform (FFT). Besides, they can also be directly determined based on the video captured by the high-speed camera introduced in section 2.2.3. Figure 11 presents f_p and the associated f_p^*, i.e., the normalized frequency defined as $f_p^* = f_p l/U_\infty$. For comparison, the dominant spanwise vortex shedding frequency f_s and f_s^* are also given in figure 11. For the case with $l^* = 1/2$, the flapping frequency f_p values from c_p and high-speed video are compared in figure 11(a), using the symbols of solid and hollow circles, respectively. Obviously, the f_p obtained from the two methods almost

overlaps with each other, thus only the f_p determined with c_p are given for all other cases for simplicity, as shown in figure 11.

Apparently, U_{cr} decreases rapidly with increasing l^* and becomes approximately constant at $l^* > 1$ for the presently tested range of U_∞. As expected, once the plate flapps at $U_\infty > U_{cr}$, the flapping frequency f_p increases almost linearly with increasing U_∞ for all l^* values. This observation is qualitatively similar to that reported for a flag or flexible plate aligned along the streamwise direction (Huang and Sung, 2010; Virot et al. 2013; Watanabe et al. 2002; Yu et al. 2019). For a standard flag, the dominant flapping frequency grows linearly with increasing U_∞, with a discontinuity as the flapping mode switches at critical U_∞, which depends on the length-to-width ratio of the flag (Virot et al. 2013).

Considering the linear dependence of f_p on U_∞ for a streamwise aligned flexible plate in a uniform flow, the corresponding f_p^* keeps constant unless its flapping mode switches (Shelley et al. 2005; Virot et al. 2013). For the present tested flexible plate bent along the streamwise direction, the dependence of f_p^* on l^* is given in figure 11(b). The behavior of f_p^* is more complicated relative to that of a streamwise-aligned flexible plate. For the shorter plate with $l^* = 1/2$ and $5/8$, f_p^* decreases monotonically and approaches a constant value with increasing U_∞. On the other hand, for the relatively longer plates with $l^* \geq 3/4$, f_p^* reduces initially with increasing U_∞. With further increasing U_∞, f_p^* increases and reaches a stable value after the presence of the minimal value. As shown in figure 11, the final stable f_p^* occurring at relatively higher U_∞ is generally larger for a flexible plate with larger l^*, which is qualitatively consistent with that observed for a streamwise-aligned standard flexible plate (Huang and Sung, 2010). Considering the variation of the aerodynamic forces with increasing U_∞, (figure 4), it may be concluded that the aerodynamic forces on the finite cylinder are remarkably modulated once the plate starts flapping, while the flapping mode and frequency do not have significant effects on this modulation.

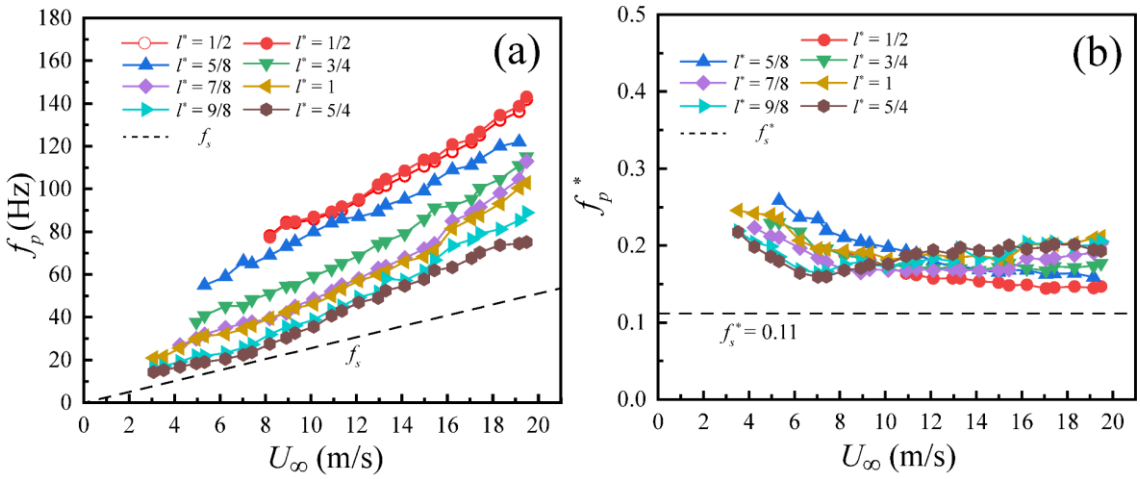

Figure 11 Flapping frequency of the flexible film at the cylinder free end: (a) real frequency f_p, (b) normalized frequency f_p^*.

3.3 Near-wake structures

Figure 12 presents the flow visualization results in the central lateral plane, i.e., $y^* = 0$, for different cases. For the uncontrolled case at $U_\infty = 5$ m/s (figure 12a), the free-end shear flow is stable initially, which overshoots the free end. The Kelvin-Helmholtz (K-H) instability appears in this shear flow. For the case with $l^* = 1/2$ at $U_\infty = 5$ m/s (figure 12b), the plate is statically deformed, bent downstream by the free-end shear flow. As expected, this statically deformed plate does not change the free-end shear flow noticeably, except that the K-H instability becomes more violent downstream the cylinder at approximately $x^* > 2$. This enhanced K-H instability may be ascribed to the possible small perturbation introduced by the flexible plate since it cannot be perfectly steady in the shear flow. A close look at the shear flow above the free end can confirm that the steady bented plate acts to upraise the free-end shear flow, as shown in figure 12(a & b). This scenario to some extent is equivalent to a case with an increased aspect ratio of the cylinder, and thus slightly increases the aerodynamic forces of the cylinder, which accord well with that shown in figure 4.

As U_∞ increases to 8 m/s, the plate with $l^* = 1/2$ flaps and generates a large-scale vortex in each flapping period (figure 12c), which is named 'flapping-induced vortex, FIV' hereafter (Alam and Muhammad 2020b; Chao et al. 2021). Compared with the uncontrolled case (figure 12a) and the case with the plate steady deformed (figure 12b), the flapping plate perturbates the free-end shear flow significantly. The FIVs induce more high-speed flow from the freestream into the cylinder near

wake, enhancing the momentum exchange. For the case with $l^* = 1$, the plate flaps periodically at $U_\infty = 5$ m/s (figure 12d). Apparently, the FIVs generated by the plate with $l^* = 1$ are far larger than those shown in figure 12(c) with $l^* = 1/2$, suggesting that the scale of the FIVs is approximately proportional to l^*. However, considering the results shown in figure 4, it may be concluded that the modulation of aerodynamic forces is insensitive to the scale and the frequency of the FIVs.

It is clearly observed that the FIV of $l^* = 1/2$ forms completely above the free end and hits its downstream part (figure 12c). However, the FIV of $l^* = 1$ forms behind the cylinder free end (figure 12d). This explains why C_p' presents a local peak near the center of the free end for the former case, while reaching its maximum at the trailing edge of the free end for the latter, as shown in figure 9 (b & c).

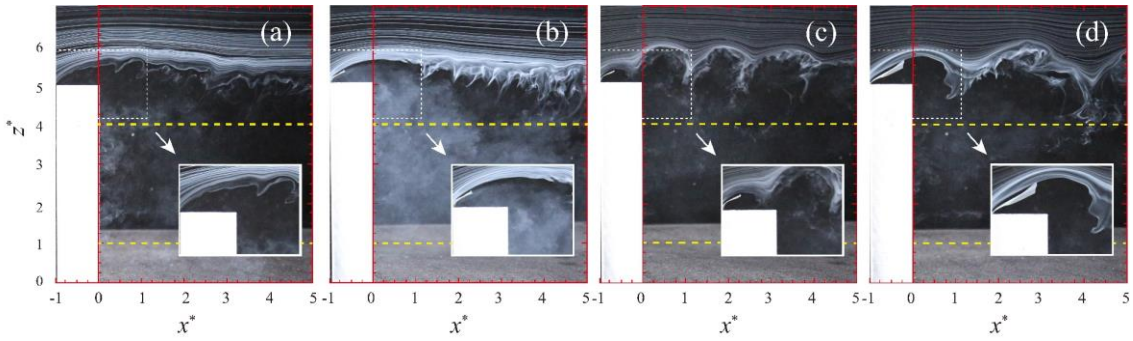

Figure 12 Flow visualization in the central lateral plane: (a) uncontrolled case, $U_\infty = 5$ m/s, (b) $l^* = 1/2$, $U_\infty = 5$ m/s, (c) $l^* = 1/2$, $U_\infty = 8$ m/s, (d) $l^* = 1$, $U_\infty = 5$ m/s (the dashed line indicates the spanwise locations of $z^* = 1$ and 4, respectively).

Figure 13 shows the flow visualization in the spanwise planes at $z^* = 1$ and 4, as marked by the dash lines in figure 12. For the sake of simplicity, only the results of the cases with $l^* = 0$ and 1 at $U_\infty = 5$ m/s are given. For $l^* = 0$(uncontrolled case), under the effect of downwash wash flow, the spanwise shear flow converges gradually as moving downstream and no alternating Karman vortex shedding presents at $z^* = 4$ (figure 13(a)). This observation is consistent with the experimental and numerical results reported in the literature (e.g. Sattari et al. 2012, Saeedi et al. 2014, Kindree et al. 2018, da Silva et al. 2020). On the other hand, alternating Karman vortex shedding presents clearly at $z^* = 1$, where the effect of downwash flow retreats. That is to say, alternating spanwise vortex shedding dominates the lower part of the finite cylinder, while it diminishes toward the free end,

suggesting that the downwash flow tends to suppress Karman vortex shedding (da Silva et al. 2020, Saha, 2013).

For the case with $l^* = 1$, the spanwise shear flow at $z^* = 4$ is converted into symmetrical vortex shedding and synchronized with the FIVs shown in figure 12(d). It suggests that the flapping plate at the free end not only modulates the free-end shear flow, but also the whole flow around the cylinder free end. As expected, this effect diminishes with decreasing z^*. At $z^* = 1$, i.e., the lower part of the cylinder, the near wake is also characterized by the alternating spanwise vortex shedding, similar to the uncontrolled case, although the wake width and vortex strength are suppressed relative to the uncontrolled case, as shown in figure 13(c & d).

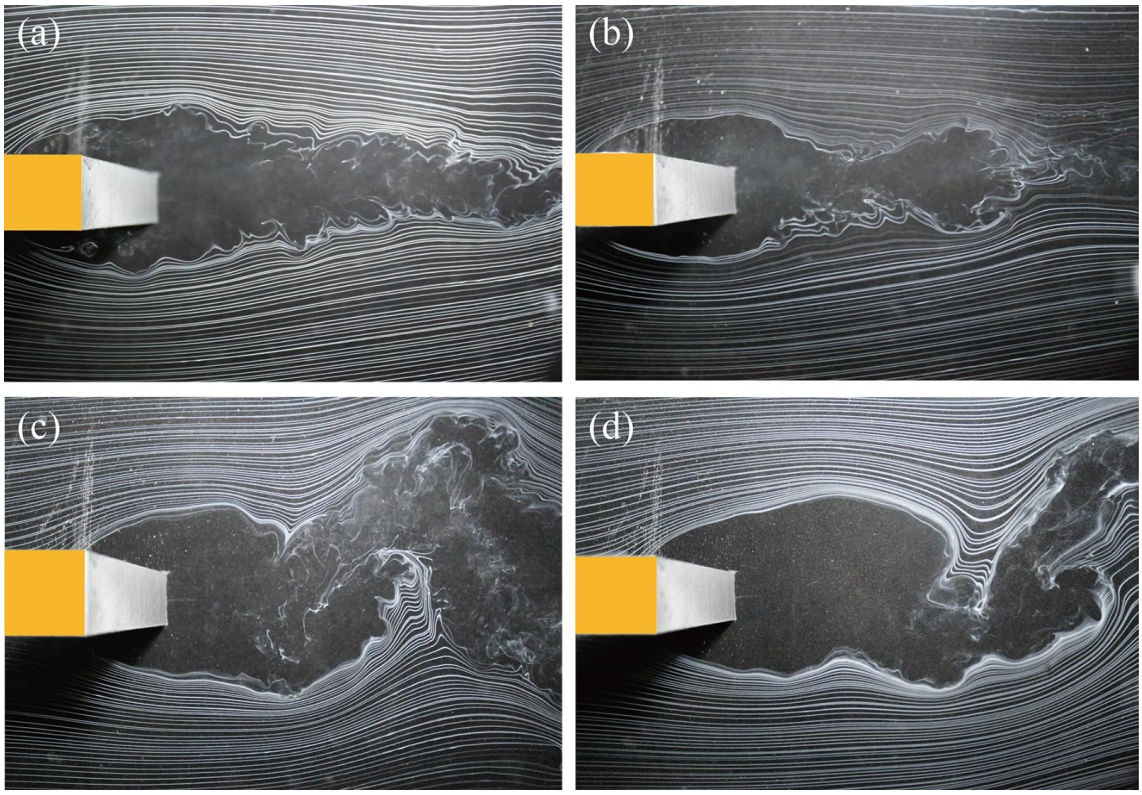

Figure 13 Flow visualization in the spanwise planes at $U_\infty = 5$ m/s: (a, b) $z^* = 4$, (c, d) $z^* = 1$. (a, c) uncontrolled case, (b, d) $l^* = 1$.

Figure 14 presents the contours of the typical instantaneous w_y^* and U^* in the central lateral plane, i.e., $y^* = 0$, for the cases identical to those shown in figure 12. Generally, the PIV measured results consistent well with those observed using the smoke wire flow visualization technique. The iso-contour of $w_y^* = -0.5$ are highlighted using dashed lines for the illustrating of FIVs in the wake. Since the present study focuses on the shear flow and vortices induced by the flapping plate, the

complex and chaotic vortex structures in the recirculation zone as reported by Wang and Zhou (2009), Rastan et al. (2021) and Saeedi et al. (2014) are removed for an easy understanding. For the case with l^* = 1/2 at U_∞ = 5 m/s (figure 14b & f), the shear flow from the free end is initially stable, crossing over and forming a downwash behind the cylinder, which is the same as in the uncontrolled case shown in figure 14(a & e). This observation confirms again that the steady deformed plate at the free-end leading edge does not change the flow around the finite square cylinder noticeably. Once the flexible plate flaps (figure 14c & g, d &h), obvious FIVs emerge in the shear flow, consistent with that observed in figure 12. It can be clearly observed FIVs in the wake for case l^* = 1 at U_∞ = 5 m/s are larger than that for case l^* = 1/2 at U_∞ = 8 m/s, and with a longer distance among vortices indicating a relative low flapping frequency which agrees well with results in figure 11. It is interesting to note that FIVs locate on the margin of the high-speed flow delivering high-speed flow (red color) from the free stream into the near wake region (green and blue color), which act to suppress the flow reversal zone near the cylinder free end, while elongating it at the lower part of the cylinder (figures 14 c & g, h & d).

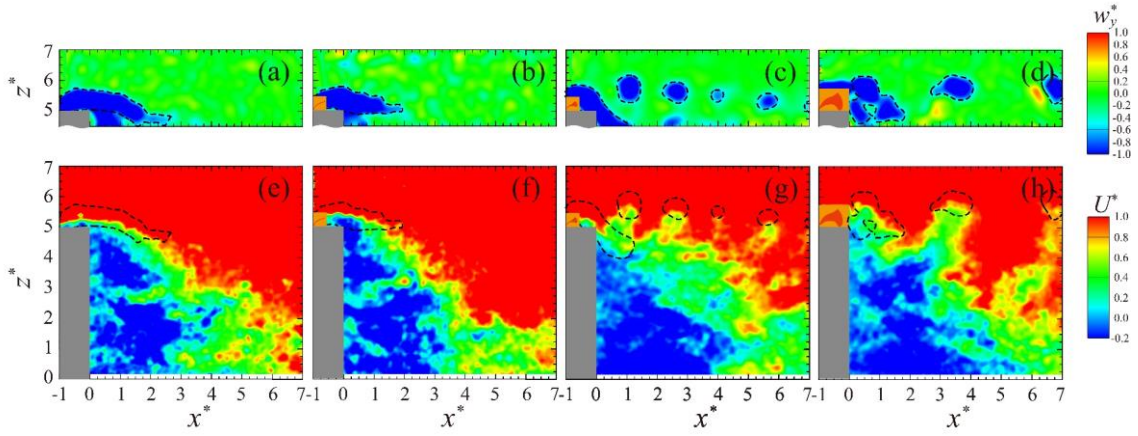

Figure 14 Contours of (a, b, c, d) vorticity w_y^* and (e, f, g, h) instantaneous U^* in the central lateral plane: (a, e) uncontrolled case, U_∞ = 5 m/s, (b, f) l^* = 1/2, U_∞ = 5 m/s, (c, g) l^* = 1/2, U_∞ = 8 m/s, (d, h) l^* = 1, U_∞ = 5 m/s, the iso-contour lines of w_y^* = -0.5 are also depicted with dashed line.

It is interesting to evaluate the time-averaged near wake structures to reveal the effects of the plate of different lengths. Figure 15 gives the time-averaged sectional streamlines in the y^* = 0 plane, overlapped with the contours of $\overline{U^*}$. For the uncontrolled case shown in figure 15(a), both the

streamlines and the flow reversal zone are very similar to those reported by Wang and Zhou (2006) and Zhao et al. (2021) for a finite square cylinder with H/d = 5, immersed in a thin boundary layer. The near wake is dominated by the downwash flow, which extends close to the bottom wall, forming a saddle point (marked with a red cross) at $z^* \approx 0.81$ by clashing with the upwash flow. Although the steady deformed plate with l^* = 1/2 slightly uplifts the shear flow above the free end, it does not change the near wake structure significantly, as shown in figure 15(b). This observation is consistent with the free-end shear flow observed in figures 12(b) and 14(b), compared with the uncontrolled case.

Once the flexible plate flaps (figure 15c, d), the FIVs change the mean near wake structures substantially relative to the uncontrolled case. Firstly, the FIVs entrain more high-speed flow into the near wake, suppressing the flow reversal zone near the free end of the cylinder, while enlarging it at the lower part of the wake. For example, the maximum streamwise extent of the flow reversal zone enlarges from 2.75 d (the uncontrolled case) to 3.75 d. Secondly, the downwash flow is enhanced relative to the uncontrolled case, shifting the saddle point to a lower position at $z^* \approx 0.50$. Thirdly, the free-end shear flow extends further downstream, relative to that of the uncontrolled case, resulting in the upward flow near the cylinder rear face and forming a swirl flow downstream the cylinder (figures 15c & d).

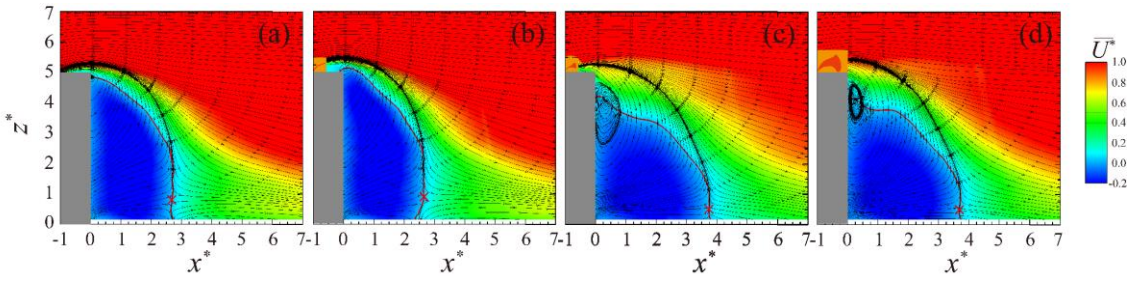

Figure 15 Time-averaged sectional streamlines and contours of $\overline{U^*}$ in the central lateral plane: (a) uncontrolled case, U_∞ = 5 m/s, (b) l^* = 1/2, U_∞ = 5 m/s, (c) l^* = 1/2, U_∞ = 8 m/s, (d) l^* = 1, U_∞ = 5 m/s. The red solid line indicates $\overline{U^*}$ = 0.

Figure 16 gives the time-averaged contours of $\overline{U^*}$ in the spanwise planes at z^* = 1 and 4 for the cases identical to those shown in figure 15. Similar to that observed in the lateral plane at y^* = 0 (figures 12, 14 & 15), the steady deformed flexible plate has negligible effects on the time-average near wake structure compared to the uncontrolled case, except the slightly shrunk flow reversal zone

at $z^* = 4$, as shown figures 16 (a & b).

Once the plate flaps, e.g., $l^* = 1/2$ at $U_\infty = 8$ m/s and $l^* = 1$, $U_\infty = 5$ m/s, the flow reversal zone at $z^* = 4$ retreats obviously near the wake centerline, forming a M-shape low-speed region, as shown in figures 16(c & d). The $\overline{U^*}$ near the wake centerline increases significantly relative to that shown in figures 16(a & b), which is ascribed to the high-speed flow induced from the free stream into the near wake by the FIVs, as shown in figures 12(c & d) and figures 14(c & d). This enhanced downwash and accompanied highspeed flow extend the flow reversal zone in streamwise direction at $z^* = 1$ (figure 16g, h). Moreover, the corresponding wake is obviously suppressed, relative to that of the uncontrolled case, which consists with the flow visualization shown in figures 13(c & d).

Both the flow visualization and PIV results reveal the remarkable influence of the flapping flexible plate on the flow around the finite square cylinder, which consists well with the variation of aerodynamic forces discussed in section 3.1. Particularly, the FIVs induce highspeed flow into the near wake periodically, resulting in in-phase vortex shedding near the cylinder free end (figure 13b) and elongating the spanwise vortex shedding at the lower part of the cylinder (figure 13d).

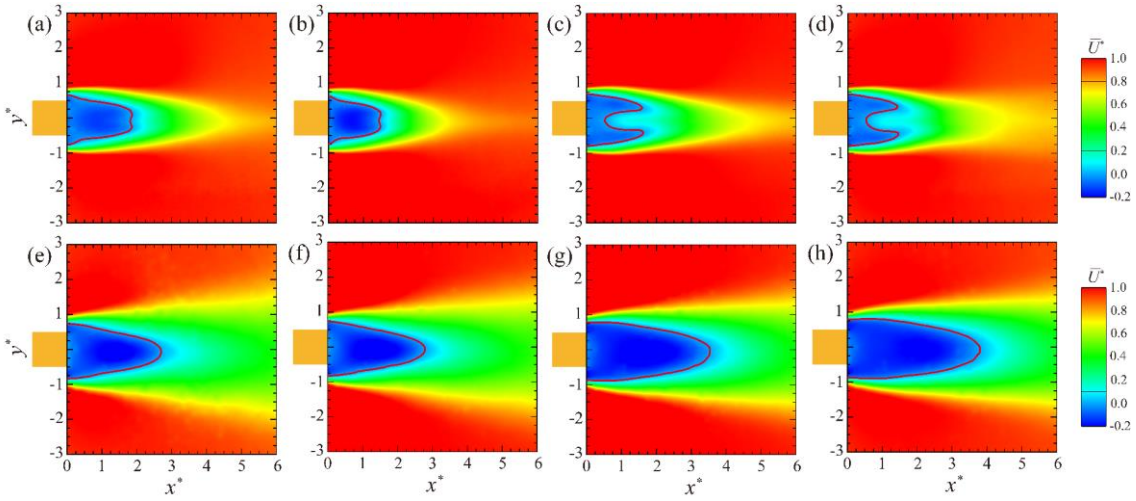

Figure 16 Time-averaged contours of $\overline{U^*}$ in the spanwise planes at (a-d) $z^* = 4$ and (e-h) $z^* = 1$: (a, e) uncontrolled case, $U_\infty = 5$ m/s, (b, f) $l^* = 1/2$, $U_\infty = 5$ m/s, (c, g) $l^* = 1/2$, $U_\infty = 8$ m/s, (d, h) $l^* = 1$, $U_\infty = 5$ m/s. The red solid line indicates $\overline{U^*} = 0$.

3.4 Discussion

Figure 17 shows the power spectra of the fluctuating pressure on the cylinder side face at different z^* values. For the uncontrolled case (figure 17a), the spectra at all z^* values present a

remarkable peak at f_s^* = 0.11, which weakens with increasing z^*, i.e., towards the free end. Apparently, this dominant peak is associated with the spanwise Karman vortex shedding. It suggests that the free-end downwash flow suppresses the spanwise vortex shedding, consisting with that reported by Fox and West (1993) and Wang et al. (2012).

For the case with l^* = 1, it is interesting to note that the spectra at different z^* values present two distinct peaks (figure 17b). At the lower part of the cylinder, i.e., $z^* \leq 3$, the peak at f_s^* = 0.11 is still observable, although significantly weakened relative to the uncontrolled case. The peak associated with the spanwise Karman vortex shedding disappears at larger z^*, while another predominant peak presents at $f_p^* \approx 0.22$ in the spectrum, and enhances gradually with increasing z^* (figure 17b). It is worth noting that f_p^* will be a different value for cases with different l^*. As discussed in section 3.2, this pronounced peak at f_p^* is caused by the plate flapping. It may be concluded that, for the case where the plate flaps, the spanwise Karman vortex shedding still appears at the lower part of the cylinder, although weakened significantly. On the other hand, the flow near the upper part of the cylinder is dominated by the flapping motion of the plate.

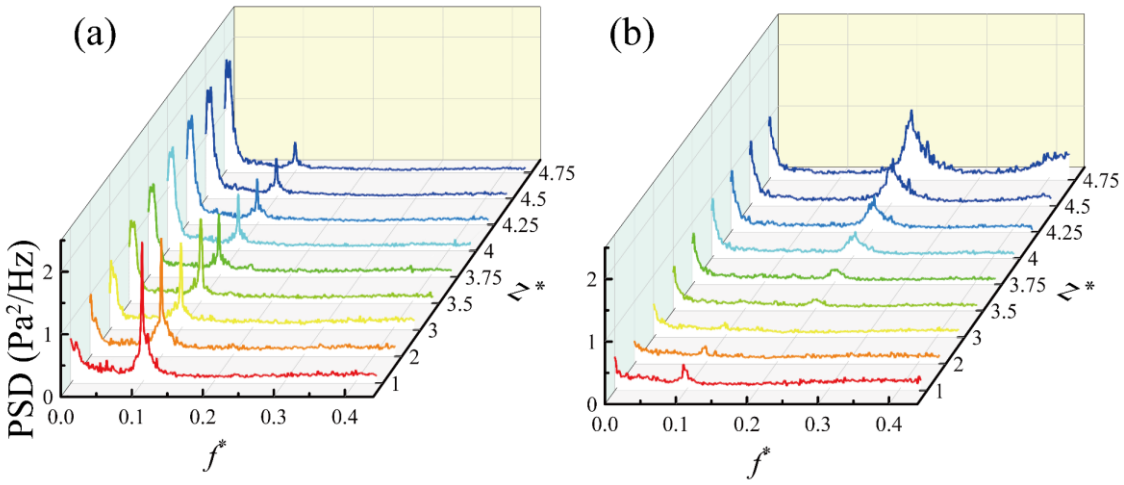

Figure 17 Power spectra of the fluctuating pressure on the cylinder side face at U_∞ = 15 m/s: (a) uncontrolled case, (b) l^* = 1.

Considering that the fluctuating pressure contains different frequency components, it is interesting to decompose it and reveal the dynamics and correlations of these typical components, which represent different physical phenomena, e.g., spanwise Karman vortex and flapping-induced vortex. Figure 18 depicts C_{p4d}, the fluctuating pressure on the cylinder side face at z^* = 4, for the

uncontrolled case with U_∞ = 15 m/s. Apparently, C_{p4d} bears both low-frequency and high-frequency components, as discussed by Kindree et al. (2018) and Peng et al. (2019). The wavelet packet filter (WPF) was used to decompose C_{p4d} into multiple components in the frequency domain. WPF is a signal filtering technique, including wavelet packet decomposition WPD and wavelet packet reconstruction WPR, respectively. Different from the conventional FFT filter, WPF can decompose the signal with a smoother margin for the components in the frequency domain and reconstruct the signal arbitrarily with the selected components, which makes it possible to extract the frequency component of interest (Coifman & Wickerhauser, 1992; Wickerhauser, 1991).

For the C_{p4d} shown in figure 18(a), a dominant peak presents at f_s^* = 0.11 (figure 18b), which is ascribed to the periodic Karman vortex shedding. A five-order WPD is performed to divide the spectrum into 32 subsections, coded from D0 to D31 as shown in figure 18(c). Each subsection contains only the characteristics of the signal within a specific frequency range. The envelope of the spectra of these 32 components coincides well with the original spectrum. The two dominant subsections associate with f_s^*, i.e., D3 and D4, are highlighted with red color, as shown in figure 18(c). Thus, D0-D2 and D5-D31 can be considered as the low-frequency and high-frequency components of C_{p4d}, respectively. Figure 18(a) presents the WPR signals using the low-frequency (D0-D2), dominant-frequency (D3+D4) and high-frequency components (D5-D31), respectively. Besides, figure 18(a) compares C_{p4d_r}, which is reconstructed using both low-frequency and dominant-frequency components (D0-D4), with the original C_{p4d}. Apparently, C_{p4d_r} almost overlaps with C_{p4d}, besides the high-frequency fluctuation, suggesting that the WPF technique is applicable in extracting the frequency components of interests.

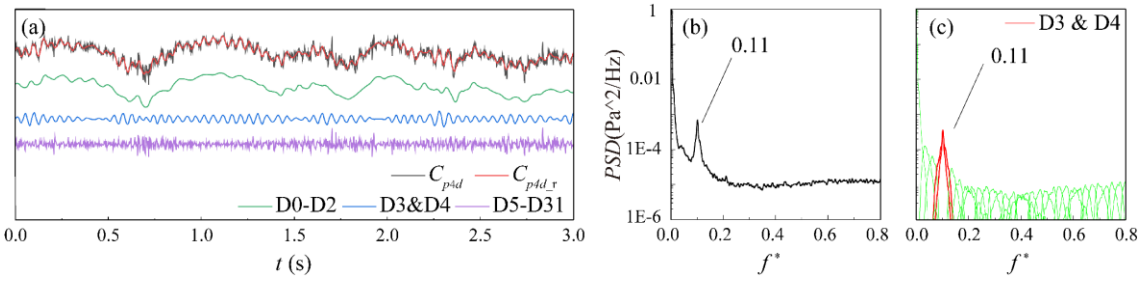

Figure 18 Comparison of the original signal, reconstructed signal, different components and the corresponding spectra for C_{p4d} at U_∞ = 15 m/s, (a) time history of C_{p4d} and corresponding reconstructed C_{p4d_r}, low-frequency components (D0-D3), dominant-frequency components

(D3+D4) and high-frequency portion (D5-D31), (b) power spectrum of C_{p4d}, (c) power spectra of different components.

For the case with $l^* = 0$ and 1 at $U_\infty = 15$ m/s, figure 19 shows the WPR C_p signals on both lateral faces and the corresponding phase lag between them. For the uncontrolled case, time histories in figures 19 (a & b) are the pressure at $z^* = 4.5$ and 1, respectively, with the dominant frequency induced by the Karman vortex shedding. It is obvious that the fluctuating amplitude of pressure at $z^* = 4.5$ is much smaller than that at $z^* = 1$, which agrees well with the result of power spectra (figure 17a). Moreover, WPR C_p on both side faces are approximately out of phase at $z^* = 4.5$ and 1, resulting in the phase lag $\Delta\theta$ of about 180° (figure19a, b).

For the case with $l^* = 1$, the WPR C_p signals at $z^* = 4.5$ and 1 correspond the frequency components at f_p^* and f_s^*, respectively (figure 19c, d). The strong synchronization of the WPR C_p signals at $z^* = 4.5$ reveals the symmetric vortex shedding induced by the flapping plate (see figure 13b). As expected, the corresponding $\Delta\theta$ is close to 0°. However, the WPR C_p on both sides of the cylinder at $z^* = 1$ are still out of phase, as shown in figure 19(d), although the magnitude of the WPR C_p is substantially suppressed, relative to the uncontrolled case.

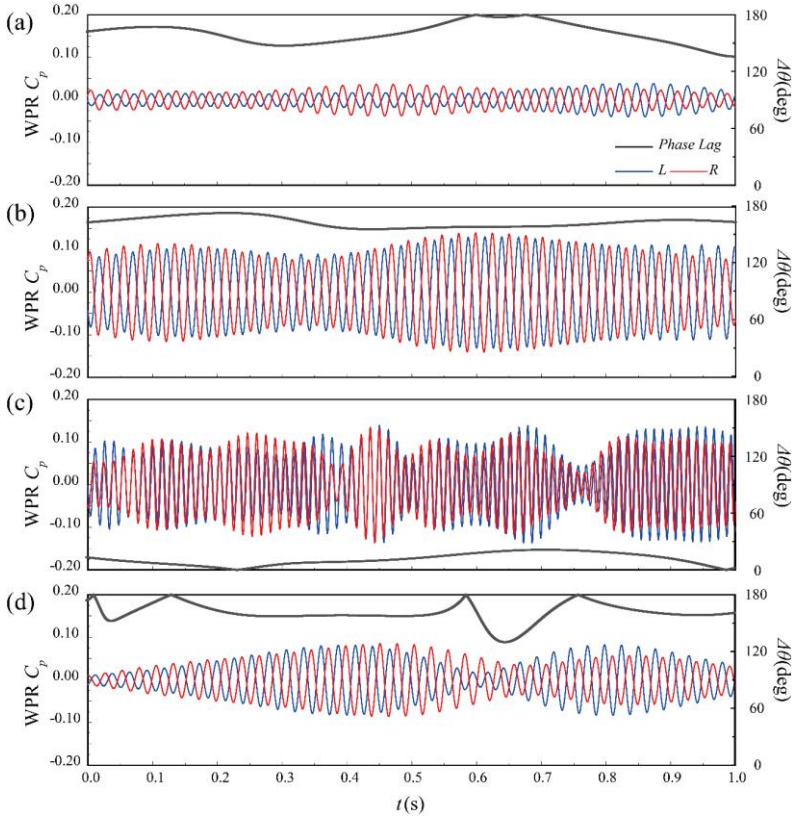

Figure 19 WPR C_p signals on the cylinder side faces with the dominant-frequency components and the phase lag between them at U_∞ = 15 m/s, (a) l^* = 0, z^* = 4.5, (b) l^* = 0, z^* = 1, (c) l^* =1, z^* = 4.5 and (d) l^* = 1, z^* = 1.

Figure 20 presents the probability density function PDF of $\Delta\theta$ for both the uncontrolled case and the case with l^* = 1 at U_∞ = 15 m/s. For the former, $\Delta\theta$ of the WPR C_p signals with f_s^* component concentrates near 180°, which suggests the prevalent out of phase Karman vortex shedding along the entire cylinder span.

For the case with l^* = 1, the PDF of $\Delta\theta$ of the WPR C_p with only the f_s^* and f_p^* components are presented in figure 20 (b & c), respectively. The WPR C_p with only the f_s^* component is approximately out of phase with $\Delta\theta$ concentrates near 180°, especially at smaller z^*. However, compared with the uncontrolled case, the peak of the PDF of $\Delta\theta$ is obviously suppressed. Moreover, the peak of the PDF reduces gradually with increasing z^*, as shown in figure 20 (b). Particularly, the peak disappears completely, and the PDF becomes almost uniformly distributed at z^* = 4 and 4.5, near the free end. On the other hand, the WPR C_p with only the f_p^* component tends to be in phase especially near the free end, as shown in figure 20(c). The observation suggests the flapping plate at the free end not only converts the spanwise vortex shedding into symmetrical near the free end, but also suppresses the anti-symmetrical Karman vortex shedding at the lower part of the cylinder.

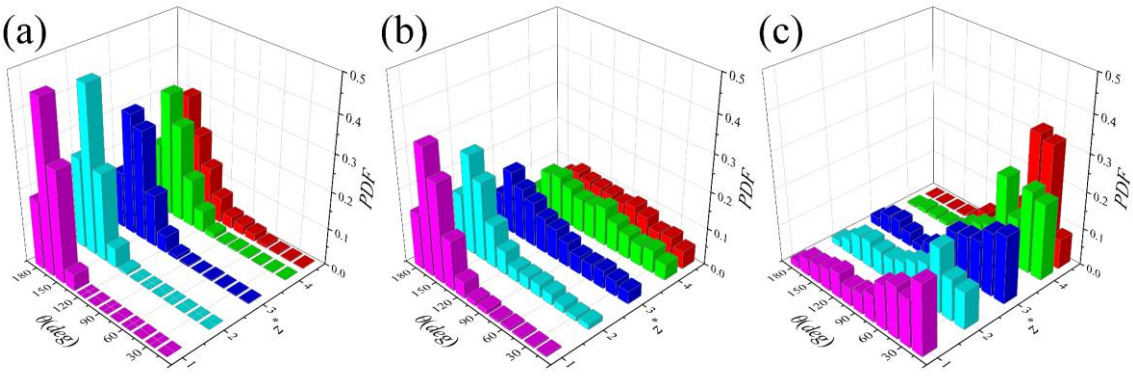

Figure 20 PDF of the phase lag between the WPR C_p signals on the cylinder side faces at U_∞ = 15 m/s, (a) l^* = 0, reserving f_s^*, (b) l^* = 1, reserving f_s^*, (c) * = 1, reserving f_p^*.

Conclusions

In the present study, the aerodynamic performance and near wake structure of a finite square cylinder with a flapping flexible plate at its free end were experimentally studied. The focus is given on the flapping behavior of the flexible plate and its effect on the flow structure around the cylinder. The investigation leads to the following conclusions.

1) The plate is statically bent along the free-end shear flow at relatively low U_∞, which does not have noticeable impacts on the flow around and aerodynamic forces of the finite cylinder. The flexible plate flaps when U_∞ reaches a critical velocity U_{cr}. The flapping plate reduces the aerodynamic forces of the finite cylinder significantly, with the maximum reduction in $\overline{C_d}$, C_d' and C_l' of 5%, 25% and 60%, respectively.

2) U_{cr} reduces gradually with the increase of the plate length. Once the plate flaps, its flapping frequency increases approximately linearly with U_∞. Large-scale flapping-induced vortices appear at the tip of the flexible plate, which enhance the downwash flow behind the cylinder and induce more high-speed flow into the near wake. The flapping plate suppresses the flow reversal zone near the cylinder free end, but enlarges it at the lower part of the cylinder.

3) The flapping plate tends to convert alternating spanwise vortex shedding from both sides of the cylinder into symmetrical shedding, especially near the free end. Moreover, it also weakens the Karman vortex shedding at the lower part of the cylinder, thus resulting in a significant reduction in the aerodynamic forces. Both the reduction in aerodynamic forces and the variation of near wake structures are insensitive to the length and flapping frequency of the flexible plate, once it starts flapping.

Acknowledgement

Authors wish to acknowledge the support given to them from the National Natural Science Foundation of China through Grants 52078505.

References:

Abdelhamid, T., Alam, M.M., Islam, M., 2021. Heat transfer and flow around cylinder: Effect of

corner radius and Reynolds number. International Journal of Heat and Mass Transfer, 171, 121105.
Alben, S., Shelley, M., Zhang, J., 2002. Drag reduction through self-similar bending of a flexible body. Nature, 420, 479-481.
Alam, M.M., Abdelhamid, T., Sohankar, A., 2020a. Effect of cylinder corner radius and attack angle on heat transfer and flow topology. International Journal of Mechanical Sciences, 175, 105566.
Alam, M.M., Muhammad, Z., 2020b. Dynamics of flow around a pitching hydrofoil. Journal of Fluids and Structures, 99, 103151.
Anderson, E. A., Szewczyk, A. A., 1997. Effects of a splitter plate on the near wake of a circular cylinder in 2 and 3-dimensional flow configuration. Experiments in Fluids, 23, 161-174.
Bai, H.L., Alam, M.M., 2018. Dependence of square cylinder wake on Reynolds number. Physics of Fluids, 30, 015102.
Bearman, P.W., 1965. Investigation of the flow behind a two-dimensional model with a blunt trailing edge and fitted with splitter plates. Journal of Fluid Mechanics, 21(2), 214-255.
Brücker, C., Weidner, C., 2014. Influence of self-adaptive hairy flaps on the stall delay of an airfoil in ramp-up motion. Journal of Fluids and Structures, 47, 31-40.
Binyet, E.M., Chang, J.Y., Huang, C.Y., 2020. Flexible Plate in the Wake of a Square Cylinder for Piezoelectric Energy Harvesting—Parametric Study Using Fluid-Structure Interaction Modeling. Energies, 13, 2645.
Bourgeois, J.A., Sattari, P., Martinuzzi, R.J., 2011. Alternating half-loop shedding in the turbulent wake of a finite surface-mounted square cylinder with a thin boundary layer. Physics of Fluids, 23, 095101.
Bourgeois, J.A., Sattari, P., Martinuzzi, R.J., 2012. Coherent vortical and straining structures in the finite wall-mounted square cylinder wake. International Journal of Heat and Fluid Flow, 35, 130-140.
Chao, L.M., Alam, M.M., Ji, C.N., 2021. Drag–thrust transition and wake structures of a pitching foil undergoing asymmetric oscillation. Journal of Fluids and Structures, 103, 103289
Chen, Y.J., Ryu, J., Liu, Y.Z., Sung, H.J., 2020. Flapping dynamics of vertically clamped three-dimensional flexible flags in a Poiseuille flow. Physics of Fluids, 32, 071905.
Coifman, R.R., Wickerhauser, M.V., 1992. Entropy-based algorithms for best basis selection. IEEE Transactions on Information Theory, 38(2), 713-718.
da Silva, B.L., Chakravarty, R., Sumner, D., Bergstrom, D.J., 2020. Aerodynamic forces and three-dimensional flow structures in the mean wake of a surface-mounted finite-height square prism. International Journal of Heat and Fluid Flow, 83, 108569.
Doaré, O., Michelin, S., 2011. Piezoelectric coupling in energy-harvesting fluttering flexible plates: linear stability analysis and conversion efficiency. Journal of Fluids and Structures, 27, 1357-1375.
Fang, Z., Gong, C.L., Revell, A., Chen, Gang., Harwood, A., O'Connor, J., 2019. Passive separation control of a NACA0012 airfoil via a flexible flap. Physics of Fluids, 31, 101904.
Farivar, D., 1981. Turbulent uniform flow around cylinders of finite length. AIAA Journal, 19(3), 275-281.
Fox, T.A., West, G.S., 1993. Fluid-Induced Loading of Cantilevered Circular Cylinders in a Low-Turbulence Uniform Flow. Part 1: Mean Loading with Aspect Ratios in the Range 4 to 30. Journal of Fluids and Structures, 7, 1-14.
Gosselin, F., de Langre, E., Machado-Almeida, B.A., 2010. Drag reduction of flexible plates by

reconfiguration. Journal of Fluid Mechanics, 650, 319-341.
Huang, W.X., Sung, H.J., 2010. Three-dimensional simulation of a flapping flag in a uniform flow. Journal of Fluid Mechanics, 653, 301-336.
Jin, Y.Q., Kim, J.T., Hong, L., Chamorro, L.P., 2018a. Flow-induced oscillations of low-aspect-ratio flexible plates with various tip geometries. Physics of Fluids, 30, 097102.
Jin, Y., Kim, J.T., Mao, Z., Chamorro, L.P., 2018b. On the couple dynamics of wall-mounted flexible plates in tandem. Journal of Fluid Mechanics, 852, R2.
Joshi, R.U., Soti, A.K., Bhardwaj, R., 2015. Numerical study of heat transfer enhancement by deformable twin plates in laminar heated channel flow. Computational Thermal Sciences, 7, 1-10.
Kawamura, T., Hiwada, M., Hibino, T., Mabuchi, I., Kumada, M., 1984. Flow around a Finite Circular Cylinder on a Flat Plate: Cylinder height greater than turbulent boundary layer thickness. Bulletin of Jsme, 27, 2142-2151.
Kikuchi, H., Tamura, Y., Ueda, H., Hibi, K., 1997. Dynamic wind pressures acting on a tall building model - proper orthogonal decomposition. Journal of Wind Engineering and Industrial Aerodynamics, 69-71, 631-646.
Kindree, M.G., Shahroodi, M., Martinuzzi, R.J., 2018. Low-frequency dynamics in the turbulent wake of cantilevered square and circular cylinders protruding a thin laminar boundary layer. Experiments in Fluids, 59, 186.
Leclercq, T., Peake, N., de Langre, E., 2018. Does flutter prevent drag reduction by reconfiguration? Proc. R. Soc. A., 474, 20170678.
Lee, J.B., Park, S.G., Kim, B., Ryu, J., Sung, H.J., 2017. Heat transfer enhancement by flexible flags clamped vertically in a Poiseuille channel flow. International Journal of Heat and Mass Transfer, 107, 391-402.
Lee, J.B., Park, S.G., Sung, H.J., 2018. Heat transfer enhancement by asymmetrically clamped flexible flags in a channel flow. International Journal of Heat and Mass Transfer, 116, 1003-1015.
Li, S.Q., Luo, Z.B., Deng, X., Peng, W.Q., Liu, Z.Y., 2021. Experimental investigation on active control of flow around a finite-length square cylinder using dual synthetic jet. Journal of Wind Engineering and Industrial Aerodynamics, 210, 104519.
Li, Y., Li, S.Q., Zeng, L.W., Wang, H.F., 2019. Control of the VIV of a cantilevered square cylinder with free-end suction. Wind and Structures, 29(1), 75-84.
McClean, J.F., Sumner, D., 2014. An Experimental Investigation of Aspect Ratio and Incidence Angle Effects for the Flow Around Surface-Mounted Finite-Height Square Prisms. Journal of Fluids Engineering, 136, 081206.
Noda, H., Nakayama, A., 2003. Free-stream turbulence effects on the instantaneous pressure and forces on cylinders of rectangular cross section. Experiments in Fluids, 34, 332-344.
Niu, J., Hu, L.D., 2011. Drag reduction of a hairy disk. Physics of Fluids, 23, 101701.
Okamoto, T., Yagita, M., 1973. The Experimental Investigation on the Flow Past a Circular Cylinder of Finite Length Placed Normal to the Plane Surface in a Uniform Stream. Bulletin of JSME, 16, 805-814.
Orrego, S., Shoele, K., Ruas, A., Doran, K., Caggiano, B., Mittal, R., Kang, S.H., 2017. Harvesting ambient wind energy with an inverted piezoelectric flag. Applied Energy, 194, 212-222.
Park, C.W., Lee, S.J., 2004. Effects of free-end corner shape on flow structure around a finite cylinder. Journal of Fluid Structures, 19, 141-158.

Peng, S., Wang, H.F., Zeng, L.W., He, X.H., 2019. Low-frequency dynamics of the flow around a finite-length square cylinder. Experimental Thermal and Fluid Science, 109, 109877.
Rastan, M.R., Sohankar, A., Alam, M.M., 2017. Low-Reynolds-number flow around a wall-mounted square cylinder: Flow structures and onset of vortex shedding. Physics of Fluids, 29, 103601.
Rastan, M.R., Sohankar, A., Doolan, C., Moreau, D., Shirani, E., Alam, M.M., 2019. Controlled flow over a finite square cylinder using suction and blowing. International Journal of Mechanical Sciences 156, 410-434.
Rastan, M.R., Shahbazi, H., Sohankar, A., Alam, M.M., Zhou, Y., 2021. The wake of a wall-mounted rectangular cylinder: Cross-sectional aspect ratio effect. Journal of Wind Engineering and Industrial Aerodynamics, 213, 104615.
Rinoshika, H., Rinoshika, A., Fujimoto, S., 2017. Passive control on flow structure around a wall-mounted low aspect ratio circular cylinder by using an inclined hole. Journal of Fluid Science and Technology, 12, 00636.
Saeedi, M., LePoudre, P.P., Wang, B.C., 2014. Direct numerical simulation of turbulent wake behind a surface-mounted square cylinder. Journal of Fluid Structures, 51, 20-39.
Saha, A.K., 2013. Unsteady flow past a finite square cylinder mounted on a wall at low Reynolds number. Computers & Fluids, 88, 599-615.
Sakamoto, H., 1985. Aerodynamic forces acting on a rectangular prism placed vertically in a turbulent boundary layer. Journal of Wind Engineering and Industrial Aerodynamics, 18, 131-151.
Sakamoto, H., Arie, M., 1983. Vortex shedding from a rectangular prism and a circular cylinder placed vertically in a turbulent boundary layer. Journal of Fluid Mechanics, 126, 147-165.
Sattari, P., Bourgeois, J.A., Martinuzzi, R.J., 2012. On the vortex dynamics in the wake of a finite surface-mounted square cylinder. Experiments in Fluids, 52, 1149-1167.
Sohankar, A., Esfeh, M.K., Pourjafari, H., Alam, M.M., Wang, L.J., 2018. Features of the flow over a finite length square prism on a wall at various incidence angles. Wind and Structures, 26(5), 317–329.
Sharma, K. R., Dutta, S., 2020. Flow control over a square cylinder using attached rigid and flexible splitter plate at intermediate flow regime. Physics of Fluids, 32, 014104.
Shelley, M., Vandenberghe, N., Zhang, J., 2005. Heavy Flags Undergo Spontaneous Oscillations in Flowing Water. Physical Review Letters, 94, 094302.
Singh, G., Lakkaraju, R., 2019. Wall-mounted flexible plates in a two-dimensional channel trigger early flow instabilities. Physics Review E, 100, 023109.
Sumner, D., Rostamy, N., Bergstrom, D.J., Bugg, J.D., 2017. Influence of aspect ratio on the mean flow field of a surface-mounted finite-height square prism. International Journal of Heat and Fluid Flow, 65, 1-20.
Uffinger, T., Ali, I., Becker, S., 2013. Experimental and numerical investigations of the flow around three different wall-mounted cylinder geometries of finite length. Journal of Wind Engineering and Industrial Aerodynamics, 119, 13-27.
Virot, E., Amandolese, X., Hémon, P., 2013. Fluttering flags: An experimental study of fluid forces. Journal of Fluid Structures, 43, 385-401.
Wang, H.F., Peng, S., Li, Y., He, X.H., 2018. Control of the aerodynamic forces of a finite-length square cylinder with steady slot suction at its free end. Journal of Wind Engineering and Industrial

Aerodynamics, 179, 438-448.
Wang, H.F., Zhao, X.Y., He, X.H., Zhou, Y., 2017. Effects of oncoming flow conditions on the aerodynamic forces on a cantilevered square cylinder. Journal of Fluid Structures, 75, 140-157.
Wang, H.F., Zhou, Y., Mi, J., 2012. Effects of aspect ratio on the drag of a wall-mounted finite-length cylinder in subcritical and critical regimes. Experiments in Fluids, 53, 423-436.
Wang, H.F., Zeng, L.W., Alam, M.M., Guo, W., 2020. Large Eddy Simulation of the flow around a finite-length square cylinder with free-end slot suction. Wind and Structures, 30, 533-546.
Wang, H.F., Zhou, Y., 2009. The finite-length square cylinder near wake. Journal of Fluid Mechanics, 638, 453-490.
Wang, H.F., Zhou, Y., Chan, C.K., Lam, K.S., 2006. Effect of initial conditions on interaction between a boundary layer and a wall-mounted finite-length-cylinder wake. Physics of Fluids, 18, 065106.
Watanabe, Y., Suzuki, S., Sugihara, M., Sueoka, Y., 2002. An Experimental Study of Paper Flutter. Journal of Fluid Structures, 16(4), 529-542.
Wickerhauser, M., 1991. INRIA lectures on wavelet packet algorithms.
Wu, J., Qiu, Y.L., Shu, C., Zhao, N., 2014a. Flow control of a circular cylinder by using an attached flexible filament. Physics of Fluids, 26, 103601.
Wu, J., Shu, C., Zhao, N., 2014b. Numerical study of flow control via the interaction between a circular cylinder and a flexible plate. Journal of Fluids and Structures, 49, 594-613.
Yu, Y.L., Liu, Y.Z., Amandolese, X., 2019. A Review on Fluid-Induced Flag Vibrations. Applied Mechanics Reviews, 71, 010801.
Zhao, C.Y., Wang, H.F., Zeng, L.W., Alam, M.M., Zhao, X.Y., 2021. Effects of oncoming flow turbulence on the near wake and forces of a 3D square cylinder. Journal of Wind Engineering and Industrial Aerodynamics, 214, 104674.
Zheng, C.R., Zhang, Y.C., 2012. Computational Fluid Dynamics study on the performance and mechanism of suction control over a high-rise building. The Structural Design of Tall and Special Buildings, 21, 475-491.

Figures captions

Figure 1 Experimental setup: (a) tested model and arrangement of PIV measurement planes; (b) distribution of pressure tabs.

Figure 2 Oncoming flow conditions over the flat plate.

Figure 3 Instantaneous signals of the pressure transducer and laser triggering signal and typical image of the flexible film: (a) instantaneous signals; (b) image of the flapping film.

Figure 4 Overall aerodynamic forces of the finite cylinder with a flexible film at its free end: (a) $\overline{C_d}$, (b) C_d' and (c) C_l'.

Figure 5 Sectional aerodynamic forces of the finite cylinder at U_∞ = 15m/s: (a) $\overline{C_d}$, (b) C_d' and (c) C_l'.

Figure 6 Contours of $\overline{C_p}$ and C_p' on the finite cylinder at U_∞ = 15 m/s.

Figure 7 Time history of C_l, C_{p4d} and $C_{p\mathrm{T}}$ and their corresponding spectra at U_∞ = 15 m/s: (a, c) uncontrolled case, (b, d) l^* = 1.

Figure 8 Typical flapping configurations of the flexible film with l^* = 1 at U_∞ = 8 m/s. The endpoint of the film is colored by the corresponding $c_{p\mathrm{T}}$.

Figure 9 C_p' on the cylinder free end at U_∞ = 5 and 8 m/s, (a) uncontrolled case, (b) l^* = 1/2 and (c) l^* = 1.

Figure 10 Fluctuating pressure c_p on the cylinder free end and their phase relation at U_∞ = 8 m/s: (a, c) l^* = 1/2, (b, d) l^* = l.

Figure 11 Flapping frequency of the flexible film at the cylinder free end: (a) real frequency f_p, (b) normalized frequency $f_p{}^*$.

Figure 12 Flow visualization in the central lateral plane: (a) uncontrolled case, U_∞ = 5 m/s, (b) l^* = 1/2, U_∞ = 5 m/s, (c) l^* = 1/2, U_∞ = 8 m/s, (d) l^* = 1, U_∞ = 5 m/s (the dashed line indicates the spanwise locations of z^* = 1 and 4, respectively).

Figure 13 Flow visualization in the spanwise planes at U_∞ = 5 m/s: (a, b) z^* = 4, (c, d) z^* = 1. (a, c)

940 uncontrolled case, (b, d) $l^* = 1$.

941 Figure 14 Contours of (a, b, c, d) vorticity w_y^* and (e, f, g, h) instantaneous U^* in the central lateral
942 plane: (a, e) uncontrolled case, $U_\infty = 5$ m/s, (b, f) $l^* = 1/2$, $U_\infty = 5$ m/s, (c, g) $l^* = 1/2$, $U_\infty = 8$ m/s, (d,
943 h) $l^* = 1$, $U_\infty = 5$ m/s, the iso-contour lines of $w_y^* = -0.5$ are also depicted with dashed line.

944 Figure 15 Time-averaged sectional streamlines and contours of $\overline{U^*}$ in the central lateral plane: (a)
945 uncontrolled case, $U_\infty = 5$ m/s, (b) $l^* = 1/2$, $U_\infty = 5$ m/s, (c) $l^* = 1/2$, $U_\infty = 8$ m/s, (d) $l^* = 1$, $U_\infty = 5$
946 m/s. The red solid line indicates $\overline{U^*} = 0$.

947 Figure 16 Time-averaged contours of $\overline{U^*}$ in the spanwise planes at (a-d) $z^* = 4$ and (e-h) $z^* = 1$: (a,
948 e) uncontrolled case, $U_\infty = 5$ m/s, (b, f) $l^* = 1/2$, $U_\infty = 5$ m/s, (c, g) $l^* = 1/2$, $U_\infty = 8$ m/s, (d, h) $l^* = 1$,
949 $U_\infty = 5$ m/s. The red solid line indicates $\overline{U^*} = 0$.

950 Figure 17 Power spectra of the fluctuating pressure on the cylinder side face at $U_\infty = 15$ m/s: (a)
951 uncontrolled case, (b) $l^* = 1$.

952 Figure 18 Comparison of the original signal, reconstructed signal, different components and the
953 corresponding spectra for C_{p4d} at $U_\infty = 15$ m/s, (a) time history of C_{p4d} and corresponding
954 reconstructed C_{p4d_r}, low-frequency components (D0-D3), dominant-frequency components
955 (D3+D4) and high-frequency portion (D5-D31), (b) power spectrum of C_{p4d}, (c) power spectra of
956 different components.

957 Figure 19 WPR C_p signals on the cylinder side faces with the dominant-frequency components and
958 the phase lag between them at $U_\infty = 15$ m/s, (a) $l^* = 0$, $z^* = 4.5$, (b) $l^* = 0$, $z^* = 1$, (c) $l^* = 1$, $z^* = 4.5$
959 and (d) $l^* = 1$, $z^* = 1$.

960 Figure 20 PDF of the phase lag between the WPR C_p signals on the cylinder side faces at $U_\infty = 15$
961 m/s, (a) $l^* = 0$, reserving f_s^*, (b) $l^* = 1$, reserving f_s^*, (c) $^* = 1$, reserving f_p^*.